JGR Solid Earth

RESEARCH ARTICLE
10.1029/2019JB018408

Inversion of Time-Lapse Seismic Reservoir Monitoring Data Using CycleGAN: A Deep Learning-Based Approach for Estimating Dynamic Reservoir Property Changes

Zhi Zhong[1,2], Alexander Y. Sun[2], and Xinming Wu[2,3]

[1]Key Laboratory of Tectonics and Petroleum Resources, Ministry of Education, China University of Geosciences, Wuhan, China, [2]Bureau of Economic Geology, Jackson School of Geosciences,The University of Texas at Austin, Austin, TX, USA, [3]School of Earth and Space Sciences, University of Science and Technology of China, Hefei, China

Key Points:
- We develop a cycle generative adversarial neural network (CycleGAN) model for time lapse seismic data inversion in carbon storage reservoirs
- CycleGAN combines reservoir simulation and rock physics inversion to invert high-resolution maps of CO_2 saturation from acoustic impedance
- We show that CycleGAN can successfully identify the bidirectional mappings between CO_2 saturation changes and acoustic impedance changes

Supporting Information:
- Supporting Information S1
- Movie S1
- Movie S2
- Movie S3

Correspondence to:
A. Y. Sun and Z. Zhong,
Alex.sun@beg.utexas.edu;
zhi.zhong@beg.utexas.edu

Citation:
Zhong, Z., Sun, A. Y., & Wu, X. (2020). Inversion of time-lapse seismic reservoir monitoring data using CycleGAN: A deep learning-based approach for estimating dynamic reservoir property changes. *Journal of Geophysical Research: Solid Earth*, *125*, e2019JB018408. https://doi.org/10.1029/2019JB018408

Received 20 JUL 2019
Accepted 13 FEB 2020
Accepted article online 14 FEB 2020

Abstract Carbon capture and storage is being pursued globally as a geoengineering measure for reducing the emission of anthropogenic CO_2 into the atmosphere. Comprehensive monitoring, verification, and accounting programs must be established for demonstrating the safe storage of injected CO_2. One of the most commonly deployed monitoring techniques is time-lapse seismic reservoir monitoring (also known as 4-D seismic), which involves comparing 3-D seismic survey data taken at the same study site but over different times. Analyses of 4-D seismic data volumes can help improve the quality of storage reservoir characterization, track the movement of injected CO_2 plume, and identify potential CO_2 spillover/leakage from the storage reservoirblue. However, the derivation of high-resolution CO_2 saturation maps from 4-D seismic data is a highly nonlinear and ill-posed inverse problem, often requiring significant computational effort. In this research, we apply a physics-based deep learning method to facilitate the solution of both the forward and inverse problems in seismic inversion while honoring physical constraints. A cycle generative adversarial neural network (CycleGAN) model is trained to learn the bidirectional functional mappings between the reservoir dynamic property changes and seismic attribute changes, such that both forward and inverse solutions can be obtained efficiently from the trained model. We show that our CycleGAN-based approach not only improves the reliability of 4-D seismic inversion but also expedites the quantitative interpretation. Our deep learning-based workflow is generic and can be readily used for reservoir characterization and reservoir model updates involving the use of 4-D seismic data.

1. Introduction

Carbon capture and storage (CCS) represents a viable option for mitigating anthropogenic greenhouse gas emissions from major industrial emitters, such as coal-fired power plants and chemical processing plants. The ultimate goal of all CCS projects is to achieve safe and effective storage of the injected CO_2 through various structural and geochemical trapping mechanisms while mitigating the potential leakage risks (Castelletto et al., 2013; Fu et al., 2017; Haszeldine, 2009; Jiang, 2011; Zhong, Carr, et al., 2019). Toward this goal, monitoring, verification, and accounting techniques constitute a critical component of risk management strategies for commercial-scale CCS projects, in order to demonstrate the efficacy of CO_2 trapping during both injection and postclosure periods (Zhong, Carr, et al., 2019).

Time-lapse seismic monitoring, or better known as 4-D seismic, represents one of the most widely used noninvasive monitoring, verification, and accounting techniques for tracking the movement of CO_2 plumes in carbon storage reservoirs (Johnston, 2010; Lumley, 2010). In 4-D seismic, repeated 3-D seismic surveys are taken over different times at the same location(s). By monitoring the time-lapse values of measured seismic properties (e.g., travel time, reflection amplitude, and seismic velocity), changes in the elasticity of the reservoir can be detected which, in turn, can be related to changes in reservoir properties (lithology, fluid content/saturation, and pore pressure). The ability to image injected CO_2 plume with 4-D seismic depends on the magnitude of seismic responses to CO_2 and the seismic noise level. In general, favorable conditions for conducting 4-D seismic depend on the bulk and shear moduli, as well as the bulk density of the reservoir. The more compressible the rock matrix (e.g., unconsolidated sand or fractured reservoirs) and the larger the compressibility contrast between the fluids of interest (e.g., water and CO_2), the larger the 4-D seismic

signal (Lumley, 2010). Specifically, existing studies have shown that 4-D seismic is most effective in regions of appearing or disappearing gas phase, because the pore fluid compressibility increases dramatically when the reservoir liquid in place is displaced by a more compressible liquid/gas such as CO_2 (Wang, 1997). In CCS, Norway's Sleipner field is a well-known example for successful 4-D seismic applications because of its favorable reservoir conditions (unconsolidated sand) (Arts et al., 2004; Chadwick et al., 2009).

Estimation of reservoir property changes based on the 4-D seismic data plays a vital role in reservoir characterization, through which continuous reservoir model updates can be performed, particularly for those fields that have permanent reservoir monitoring systems installed (Cao & Roy, 2017; Johansen et al., 2013). Two types of problems are generally associated with this reservoir property estimation process. In the forward problem, seismic attributes are simulated by using a rock physics model (RPM) (e.g., Gassmann-Wood and Gassmann-Hill models) that relates effective rock elastic properties to fluid saturation distributions. A good RPM can provide reliable predictions of the elastic rock properties when reservoir properties are perturbed (Johansen et al., 2013). In the inverse problem, reservoir property changes are inferred from 4-D seismic data. However, geophysical inversion is often an underdetermined problem and can be hardly solved because the information required for resolving the complex subsurface parameters often far exceeds the information we have in the recorded data. Thus, like many ill-posed inverse problems commonly seen in geophysical researches, we either need to reduce the subsurface model parameters significantly or add additional regularization constraints, before geophysical inversion can be conducted. However, these approximations may significantly reduce the accuracy and reliability of the inversion results (Dadashpour et al., 2007; Sun & Sun, 2015; Tarantola, 2005).

Different methods have been proposed to estimate the dynamic reservoir property changes based on the 4-D seismic data, which fall into two categories, deterministic and stochastic methods. Johansen et al. (2004) proposed an inverse rock physics modeling framework to numerically reconstruct rock properties by using seismic data as inputs. Assunção et al. (2016) applied a stochastic seismic inversion method to select the best match of dynamic property change maps, including pressure change and water saturation variations, that are calculated from 4-D seismic and forward simulations. Tian and MacBeth (2015) proposed a Bayesian 4-D seismic inversion workflow for reservoir characterization by combining static loop and dynamic loop methods together, which not only reduces the nonuniqueness of the 4-D seismic inversion but also avoids the rescaling issues. Grana and Mukerji (2015) proposed to estimate the dynamic reservoir property changes and static reservoir properties by using Bayesian inversion of 4-D seismic data. Amini and MacBeth (2018) also used a Bayesian approach to resolve oil water contact and gas oil ratio using 4-D seismic data. Maleki et al. (2018) identified the reservoir flow pattern by combining the reservoir simulation model, reservoir production data, and 4-D seismic data in the Norne field of Norway. While the large volume of 4-D seismic data provides new information for reservoir characterization, it also presents a significant challenge for seismic inversion because of large variations in physical properties (Johansen et al., 2013). Many of the aforementioned 4-D seismic inversion techniques have been developed to deal with such highly complicated and nonlinear relationship mapping from the data to subsurface model parameters. Most of the existing workflows, however, are not designed to streamline the large number of intermediate steps involved in the 4-D seismic inversion and associated postprocessing tasks (e.g., uncertainty quantification and rapid forecasting). In this work, we introduce an effective framework for 4-D seismic data inversion, which not only streamlines many steps in the 4-D seismic inversion but also helps to perform rapid reservoir assessment under geologic uncertainty.

Instead of calculating the reservoir property changes by repeating the forward and inverse processes iteratively as is often done in many traditional inversion methods, in this work we formulate a unified deep learning-based framework by using a cycle generative adversarial neural network (CycleGAN) model (Zhu et al., 2017). The original generative adversarial network (GAN) proposed by Goodfellow et al. (2014) provides a powerful unsupervised and semisupervised learning framework for learning the data generation process of training samples. Data generative process learning is inherent in many Bayesian inversion methods, for which the goal is to find the posterior distribution of the target variables by incorporating prior knowledge and observations. GAN approaches this problem through the so-called adversarial learning by using two competing models, a generator and a discriminator. The generator attempts to create fake data samples that are as close as possible to the training data distribution, while the discriminator tries to distinguish the fake samples from the true samples (i.e., observations). At convergence, the discriminator is maximally confused and cannot tell the fake samples from the true samples. So far, GAN has been shown to

be a more robust classifier in image segmentation problems,which can achieve significantly lower misclassifying rates than most end-to-end deep learning neural nets, especially when the training data are noisy and/or limited (Goodfellow et al., 2014; Samangouei et al., 2018; Zhong, Sun, Yang, & Ouyang, 2019) (Note: in the current context the term "end-to-end" means that the input data are transformed directly into an output prediction, bypassing the intermediate steps that usually occur in a traditional machine learning pipeline, such as feature extraction). Such a property of GAN can be extremely useful for mitigating the so-called adversarial attack phenomenon, which refers to the susceptibility of trained deep neural networks to misclassification when only a slight amount of noise is added to training samples (Szegedy et al., 2013). We note that several strategies exist for improving robustness of trained models. For example, Ganin et al. (2016) proposed to add a small amount of noise to the training images to improve the classification accuracy of neural networks. "Dropout" introduced by Hinton et al. (2012) is another way to randomize the weight of neural networks to improve its generalization performance. In many geophysical problems, the measurements are usually noisy. Thus, the same robustness property is also highly desirable for solving inverse problems in the geophysics domain. Conventional methods tackle the nonuniqueness of inverse problems by incorporating additional constraints through either deterministic strategies (Tikhonov regularization) or statistical strategies (prior distribution and likelihood function); oftentimes, the goal is to find an optimal solution that best fits the given data. In contrast, the adversarial learning capability of GAN helps it to learn data distributions without requiring explicit assumptions from the end users with regard to error distributions (Goodfellow et al., 2016), which can be hard to get.

The original GAN is designed to learn a functional mapping between a low-dimensional input space (e.g., a 1-D noise vector) and a high-dimensional data space. A large number of variants of the original GAN have been introduced in the literature since the work of Goodfellow et al. (2014). For example, Radford et al. (2015) proposed a deep convolution GAN (DC-GAN) and Ledig et al. (2017) proposed a superresolution GAN (SRGAN) to reconstruct high-resolution images. Liu and Tuzel (2016) applied coupled GAN (Co-GAN), and Yi et al. (2017) used DualGAN for cross-domain learning, which transfers the knowledge learned from a source domain to a target domain for inference. Mosser et al. (2018) applied CycleGAN to learn the forward and inverse mappings between geological model and seismic velocity model and tested the trained CycleGAN on Marmousi-2 synthetic seismic data. Dramsch et al. (2019) utilized near, middle, and far (in terms of offset angles) seismic and pore volume as inputs to invert pressure and fluid saturation changes via an autoencoder network. Other related works include the spatial GAN (SGAN) proposed by Laloy et al. (2018), which was used to generate 2-D and 3-D unconditional geological models via a training image. Chan and Elsheikh (2018) introduced a method to obtain a parameterization by extending the generator network of the GAN through stacking a second inference network that learns to perform the conditioning.

In this study, our main interest is to adapt the CycleGAN, introduced by Zhu et al. (2017), for end-to-end cross-domain learning. CycleGAN was originally designed to learn the forward and inverse mappings between two high-dimensional domains. Recently, Sun (2018) demonstrated the feasibility of using a CycleGAN-like architecture to learn the state-parameter bidirectional mappings as prescribed in a stochastic partial differential equation, opening the door for handling a large class of similar problems in geosciences. In this work, CycleGAN is used for 4-D seismic data inversion in the context of CO_2 plume tracking. We show that the proposed CycleGAN can be used to estimate the reservoir fluid property (e.g., CO_2 saturation) changes using 4-D seismic data at a high accuracy and efficiency, as compared to some traditional methods that may be insensitive to CO_2 saturation beyond a certain threshold (Zhu et al., 2019). The seismic impedance such as acoustic impedance (AI) can be calculated for each reservoir model grid cell, forming an image that has the same spatial dimensions as the reservoir property image (i.e, on the same grids). Thus, we choose the seismic impedance domain and reservoir property domain as two domains in this research. In the following, we first briefly introduce the basic principles behind CycleGAN and the RPMs in section 2. Then we demonstrate the use of a CycleGAN-based workflow for 4-D seismic data inversion in section 3. Finally, conclusions and summaries are provided in the last section.

2. Materials and Methods

In this section, we describe the methods for time-lapse seismic forward modeling, the RPMs, and the CycleGAN-based bidirectional learning. To facilitate the discussion, we first describe the use case for our study, which is concerned with the CO_2 plume tracking in a sandstone reservoir.

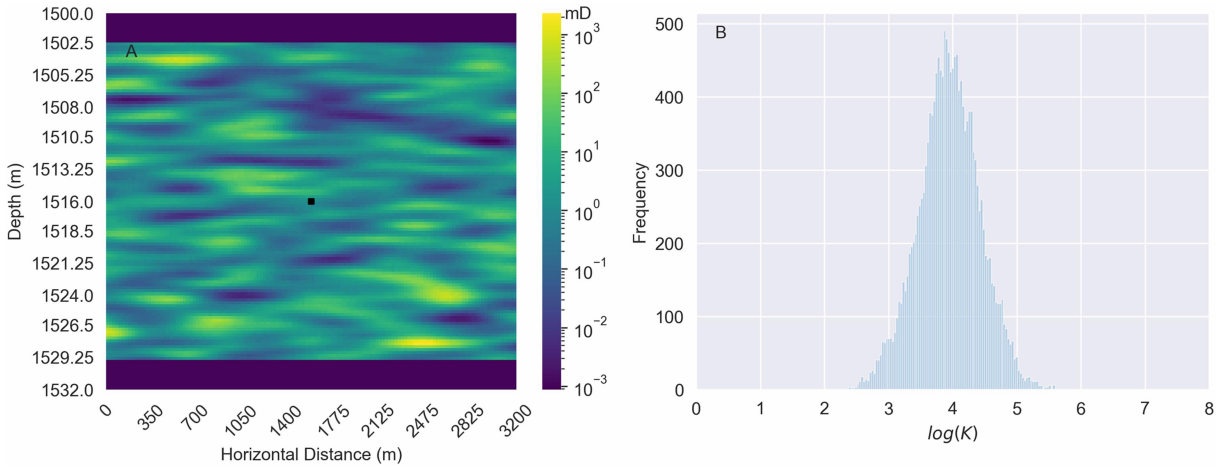

Figure 1. (a) A sample stochastic permeability field of the synthetic 2-D geological reservoir model (a vertical section) generated by using sequential Gaussian simulation for the base case, where the block square corresponds to injector location and three sections are included in this model, namely, the upper shale, middle sandstone, and lower shale sections. (b) Histogram of the permeability field. Note that the upper and lower sections of the reservoir are excluded when calculating the permeability histogram.

2.1. Geological Model

The geological model considered in this study is a 2-D vertical slice of a synthetic saline aquifer, which is discretized uniformly by a 128×128 grid (i.e., 128 grid blocks in x and z directions and a single layer in the y direction) (Figure 1). The width (Δx) and length (Δy) of each grid block are both set to 25 m, and the height (Δz) of each grid block is 0.25 m. Thus, the resulting reservoir model is 3,200 m along the x direction, 25 m along the y direction, and 32 m in the vertical direction. The reservoir model is divided into three sections along the vertical direction. The upper (layers 1 to 10 from the top) and the lower sections (layers 118 to 128) are shale layers and serve as reservoir seals. The middle section (layers 11 to 118) corresponds to a sandstone formation and provides the storage body for the injected CO_2. The top of the reservoir is at 1,500 m from the ground surface, at which depth the injected CO_2 is assumed to stay in the supercritical state. CMG-GEM uses the Peng-Robinson equation of state (Peng & Robinson, 1976) to model phase behavior of the oil and gas phases. Table 1 summarizes all parameters used in generating the geological model.

For the storage section of the reservoir, both permeability and porosity are assumed to be heterogeneous and are generated via geostatistical simulation methods. The distribution of permeability is assumed to be lognormal with mean (μ) of log(50 mD) and standard deviation (σ) of 0.5. The porosity distribution is assumed to be linearly correlated with log permeability and is calculated from the simulated permeability map using the following relationship

$$\phi = 0.05(\log k + 2) + 0.05, \tag{1}$$

where k denotes permeability and ϕ is porosity. The correlation lengths are 50 grid blocks (1,250 m) in the x direction and 10 grid blocks (2.5 m) in the z direction.

The shale layers (i.e., the upper and lower sections) are modeled as no-flow barriers by assigning low porosity ($\phi = 0.001$) and permeability ($k = 0.001$ mD) values to those layers. The sequential Gaussian simulation algorithm (sgsim) from the open-source software package SGeMS (Remy et al., 2009) is used to generate

Table 1
Summary of Parameters Used in Our Geological Model

Parameters	Value	Parameters	Value
$X \times Y \times Z$ (m)	$3,200 \times 25 \times 32$	Reference pressure (MPa)	15
$\delta x \times \delta y \times \delta z$ (m)	$25 \times 25 \times 0.25$	Reservoir temperature (°C)	45
$N_x \times N_y \times N_z$	$128 \times 1 \times 128$	CO_2 injection rate (m^3/day)	5×10^4

stochastic realizations of the permeability distribution. Figure 1a shows a sample realization of the generated permeability field, and Figure 1b shows its histogram. The permeability field shows more connected structures in the lateral direction than in the vertical direction, by design of geostatistical parameters used.

We emphasize, however, that deep learning models aim to extract deep representations of input data patterns and are not restricted by actual data distributions per se. Thus, our approach is not limited to the multi-Gaussian distributions assumed here, as long as the user can find a way to generate input images that reflect as much prior information as possible (Sun, 2018). Such an image-based workflow has been a cornerstone of modern geosciences, and a multitude of methods are available for generating images from input data. For example, a number of stochastic simulation methods are described in Remy et al. (2009) and Mariethoz and Caers (2014).

2.2. Fluid Model

The fluid flow system is assumed to consist of two components (brine and CO_2) and two phases (liquid and gas). The fluid flux is governed by Darcy's law

$$\mathbf{q}_\alpha = -\frac{k_{r,\alpha}\mathbf{k}}{\mu_\alpha}(\nabla P_\alpha - \rho_\alpha g \nabla z), \qquad \alpha = w, g, \tag{2}$$

where the subscript $\alpha = w, g$ denotes either the liquid phase (w) or gas phase (g), $\mathbf{q}_\alpha$ is the phase flux, $\mathbf{k}$ is absolute permeability, $k_{r,\alpha}$ is the relative permeability, and ρ_α and μ_α are the density and viscosity of each phase α. P_α is the fluid pressure of phase α, g is the gravitational constant, and z is the reservoir depth. The corresponding mass conservation equations are given by the following coupled partial differential equations

$$\frac{\partial(\phi S_\alpha)}{\partial t} = \nabla \cdot \mathbf{q}_\alpha + q_{f,\alpha,} \qquad \alpha = w, g, \tag{3}$$

where ϕ is porosity, S_α ($\alpha = w, g$) are the water and gas saturations, which are constrained by $S_w + S_g = 1$, and $q_{f,\alpha}$ are the sink/source terms. The fluid pressures of the fluid system are related through the capillary pressure $P_{c,w}$,

$$P_g = P_w + P_{c,w}. \tag{4}$$

We assume that the initial water saturation $S_{\text{init},w}$ is 0.25 in the reservoir, and the irreducible water saturation $S_{\text{ir},w}$ is 0.20. Initially, the top of the reservoir is at a pressure of 15 MPa and a constant temperature of 45 °C. An injector is located at the center of the reservoir (i.e., grid block (64, 64)), which is marked as the dark square in Figure 1a. The injection rate is fixed at 5×10^4 m^3/day and is constrained by the maximum bottom hole pressure of 200 MPa. The total injection period is 5 years. Simulated water/gas saturation maps (S_w and S_g) are saved at monthly intervals as training and testing data (Note: the data are split by realizations as described below in section 3.2). For this work, the commercial compositional reservoir simulator (CMG-GEM) (https://www.cmgl.ca/gem) is used to solve the miscible flow problem described herein. CMG-GEM discretizes equations (2) and (3) into finite-difference forms using the first-order backward differences in time and central differences in space with upstream mobility.

2.3. RPM

RPMs prescribe either analytical or empirically observed relations between rock elastic properties (e.g., velocity and impedance) and reservoir properties (e.g., fluid saturation and porosity). A large number of RPMs have been proposed in the literature (Mavko et al., 2009), which mainly differ in their underlying assumptions and the calculation of dry rock properties (Grana & Mukerji, 2015). In general, the modulus and elastic properties (such as AI) of the solid phase and dry rock and fluid phase may be calculated via the Voigt-Reuss-Hill model (Mavko et al., 2009), Wood's equation (Mavko et al., 2009), and the Hertz-Mindlin model (Dadashpour et al., 2007), for given reservoir parameters such as porosity, mineral content, and water saturation. Compressional wave velocity (P wave) is a function of bulk and shear moduli, as well as bulk density (Behzadi et al., 2011). Below, we briefly describe the RPMs used in this work.

2.3.1. The Bulk Density Model

Bulk density (ρ_b) consists of two parts, the solid rock density (ρ_m) and effective fluid density (ρ_{f_e}), which can be calculated by the following equation

$$\rho_b = \phi \sum_{\alpha=w,g} S_\alpha \rho_{f,\alpha} + (1-\phi)\sum_{j=1}^{N} f_{m(j)}\rho_{m(j)}, \tag{5}$$

Table 2
List of Density, Elastic Properties, and Fractions of Rock Minerals Used in This Study (Mavko et al., 2009)

Mineral	Fractions	Density (g/cm^3)	Bulk modulus, K (GPa)	Shear modulus, G (GPa)
Clay	0.05	2.5	21	9
Quartz	0.65	2.65	36.6	44
Feldspar	0.2	2.63	75.6	25.6
Rock fragments	0.1	2.7	80	20

where the term $\sum S_\alpha \rho_{f,\alpha}$ on the right-hand side of the equation represents the effective density of the multifluid mixture (ρ_{f_e}), $\rho_{f,\alpha}$ is the density of the individual fluid α (i.e., water and gas in the current case), S_α denotes saturation of fluid α, and ϕ is porosity; $f_m(j)$ is the volume fraction of the mineral constituent j within the solid phase of the rock; $\rho_{m(j)}$ is the density of the mineral constituent j, and N is the total number of minerals in the rock. The values of density, elastic properties, and fractions of each rock mineral used in this study are listed in Table 2.

Fluid density ($\rho_{f,\alpha}$) is a function of pressure, temperature, and salinity. In this research, the Batzle-Wang model (Batzle & Wang, 1992) is used to calculate the gas and brine density at different pressures. More details can be found in the supporting information.

2.3.2. The Compressional Wave Velocity Model

In this work, we focus on the sandstone reservoir, for which a constant cement model is widely used to calculate the bulk modulus (K_{dry}) and shear modulus (G_{dry}) for dry sandstone by assuming that the sand frame is a dense random pack of identical spherical grains with constant amounts of cement deposited at the grain surface. Thus, the P wave velocity of seismic waves can be obtained by equation (6) under the assumption of homogeneous, isotropic, and elastic media (Gassmann, 1951):

$$V_p = \sqrt{(K + \frac{4}{3}G)/\rho_b}. \tag{6}$$

The elastic modulus of the solid phase (K_{matrix}, G_{matrix}) in the rock is obtained from the Voigt-Reuss-Hill average (Hill, 1952) of the mineral constituents. This is simply the arithmetic average of the Voigt upper bound (Voigt, 1928) and the Reuss lower bound (Reuss, 1929)

$$M_{\text{VRH}} = \frac{M_{\text{Voigt}} + M_{\text{Reuss}}}{2}, \tag{7}$$

where M_{Voigt} and M_{Reuss} are the Voigt upper bound and Reuss lower bound of the elastic modulus, respectively, which are calculated as follows:

$$\begin{aligned} M_{\text{Voigt}} &= \sum_{i=1}^{N} f_{m(i)} M_{m(i)}, \\ M_{\text{Reuss}} &= \sum_{i=1}^{N} \frac{f_{m(i)}}{M_{m(i)}}, \end{aligned} \tag{8}$$

where $f_{m(i)}$ is the volume fraction of the mineral constituent i within the solid phase of the rock and $M_{m(i)}$ is the elastic moduli of the mineral constituent i.

Using the Hertz–Mindlin model (Dadashpour et al., 2007), we can obtain the dry bulk and shear moduli at the critical porosity (ϕ_c) as

$$\begin{aligned} K_{\text{HM}} &= \sqrt[\kappa]{\frac{c^2(1-\phi_c)^2 G_{\text{matrix}}^2}{18\pi^2(1-\nu)^2} P_{\text{eff}}}, \\ G_{\text{HM}} &= \frac{5-4\nu}{5(2-\nu)} \sqrt[\kappa]{\frac{3c^2(1-\phi_c)^2 G_{\text{matrix}}^2}{2\pi^2(1-\nu)^2} P_{\text{eff}}}, \end{aligned} \tag{9}$$

where K_{HM} and G_{HM} are bulk and shear modulus at critical porosity, respectively, c is the average number of contact point for each grain and its value is usually set to 9, ν is the Possion's ratio, $\kappa = 5$ is the coordination number which is determined by the reservoir type, and P_{eff} is effective pressure, which is taken as the

difference between the lithostatic $P_{\text{lithostatic}}$ and the hydrostatic pressure P (Dadashpour et al., 2007),

$$P_{\text{eff}} = P_{\text{lithostatic}} - \eta_c P, \tag{10}$$

where η_c is the coefficient of internal deformation, which is set to 1. According to Dadashpour et al. (2007), the dry rock bulk modulus (K_{dry}) and shear modulus (G_{dry}) can be defined in terms of K_{HM} and G_{HM},

$$\begin{aligned} K_{\text{dry}} &= \left(\frac{\frac{\phi}{\phi_b}}{K_{\text{HM}} + \frac{4}{3}G_{\text{HM}}} + \frac{1 - \frac{\phi}{\phi_b}}{K_{\text{matrix}} + \frac{4}{3}G_{\text{HM}}} \right)^{-1} + \frac{4}{3}G_{HM}, \\ G_{\text{dry}} &= \left(\frac{\frac{\phi}{\phi_b}}{G_{\text{HM}} + \frac{1}{6}\eta G_{\text{HM}}} + \frac{1 - \frac{\phi}{\phi_b}}{G_{\text{matrix}} + \frac{1}{6}\eta G_{\text{HM}}} \right)^{-1} - \frac{1}{6}\eta G_{\text{HM}}, \end{aligned} \tag{11}$$

where $\eta = \frac{9K_{\text{HM}}+8G_{\text{HM}}}{K_{\text{HM}}+2G_{\text{HM}}}$ and ϕ_b is the porosity at which the contact cement trend turns into constant cement trend. Note that ϕ_b is smaller than the critical porosity ϕ_c. The moduli are calculated from the contact cementation theory with $\phi_b = \phi$.

Based on the Gassmann fluid substitution theory (Gassmann, 1951), the bulk modulus (K_{sat}) and shear modulus (G_{sat}) under saturated conditions can be calculated from the dry rock moduli and solid phase moduli (Mavko et al., 2009),

$$\begin{aligned} K_{\text{sat}} &= K_{\text{dry}} + \frac{\left[1 - \frac{K_{\text{dry}}}{K_{\text{matrix}}}\right]^2}{\frac{\phi}{K_f} + \frac{1-\phi}{K_{\text{matrix}}} - \frac{K_{\text{dry}}}{K^2_{\text{matrix}}}}, \\ G_{\text{sat}} &= G_{\text{dry}}, \end{aligned} \tag{12}$$

where the subscript *matrix* denotes the solid phase in the rock and f denotes the pore fluid. In equation (12), K_f is the effective bulk modulus of the mixed fluid, which describes an isostress situation and is calculated with the Reuss low bound. In other words, fluid bulk modulus K_f gives the exact modulus of uniformly mixed fluids at fine scales (Simm, 2007):

$$\frac{1}{K_f} = \sum_{\alpha=w,g} \frac{S_\alpha}{K_{f,\alpha}}, \tag{13}$$

where $K_{f,\alpha}$ is the bulk modulus of the individual fluid α and S_α denotes the corresponding saturation. Equation (13) essentially defines the fluid bulk modulus as the weighted harmonic mean of the individual fluids. Alternatively, the Brie equation may also be used (Brie et al., 1995),

$$K_f = (K_{f,g} - K_{f,w})(S_w)^e + K_{f,g}, \tag{14}$$

where the Brie exponent (also known as the patchiness exponent), e, varying between 1 and 40, is used to represent different fluid mixtures. The P wave velocity in homogeneous, isotropic, and elastic media can be obtained from the bulk and shear moduli:

$$V_p = \sqrt{(K_{\text{sat}} + \frac{4}{3}G_{\text{sat}})/\rho_b}, \tag{15}$$

where ρ_b is the bulk density of saturated rock described in the previous section.

2.3.3. The Shear Wave Velocity Model

To calculate the S wave velocity (V_s), the empirical relations between P and S wave velocities as suggested in Castagna and Backus (1993) and Castagna et al. (1985) are used. In particular, the mudrock line in Castagna et al. (1985) is used for the shale facies

$$V_s = 0.862V_p - 1.172 \qquad \text{(km/s)}, \tag{16}$$

and the brine-saturated sandstone relationship in Castagna and Backus (1993) is adopted for the sand facies

$$V_s = 0.804V_p - 0.856 \qquad \text{(km/s)}. \tag{17}$$

The RPMs given in equations 5 and 12 suggest that rock properties depend nonlinearly on the fluid saturation S_α. The estimation of 4-D reservoir property changes from observed seismic attribute changes (V_p and V_s) is an underdetermined problem because of the large number of unknown parameters compared to limited seismic survey. Thus, additional physical constraints, including porosity distribution, lithofacies, and corresponding mineral components and compositions, are needed to constrain the estimates. The CycleGAN-based workflow, to be introduced in the next subsection, provides such a framework for combining both prior information and physical constraints, as well as for condensing intermediate steps.

2.4. CycleGAN

Cross-domain learning aims to find mappings between two implicitly related domains and is a type of supervised learning problems. Given two domains $X \in \mathbb{R}_X$ and $Y \in \mathbb{R}_Y$, where $\mathbb{R}$ denotes real space. Let the sample distributions corresponding to each domain be denoted as $p^X_{\text{data}}(x)$ and $p^Y_{\text{data}}(y)$, respectively, and let $\mathcal{G}$ denote a generative model which defines a functional mapping. Samples generated by the mapping function $\mathcal{G}_{X\to Y}$ using domain X information can be written as $\hat{y} = \mathcal{G}_{X\to Y}(x;\theta_{g,x})$, where $\theta_{g,x}$ is a set of generator parameters and $\hat{y}$ represents a generated sample. Let $\mathcal{D}_Y$ denote a discriminative model that determines whether a sample ($\hat{y}$) is from the real data distribution $p^Y_{\text{data}}(y)$ or from the generative distribution $p^{\mathcal{G}_{X\to Y}}_{\text{model}}(y)$,

$$\mathcal{D}_Y(y;\theta_{d,y}) = \begin{cases} 1, \text{ if } & y \sim p^Y_{\text{data}}(y), \\ 0, \text{ if } & y \sim p^{\mathcal{G}_{X\to Y}}_{\text{model}}(y), \end{cases} \tag{18}$$

where $\theta_{d,y}$ is a set of discriminator parameters.

The goal of the generative model ($\mathcal{G}_{X\to Y}$) is to generate fake samples but make its distribution $p^{\mathcal{G}_{X\to Y}}_{\text{model}}(y)$ as close to the original distribution, $p^Y_{\text{data}}(y)$, as possible, while the goal of $\mathcal{D}_Y$ is to distinguish samples of distribution $p^{\mathcal{G}_{X\to Y}}_{\text{model}}(y)$ from those of $p^Y_{\text{data}}(y)$ as much as possible. This is the adversarial learning problem mentioned in section 1, which was cast by Goodfellow et al. (2014) in a game-theoretic framework by solving a minimax problem.

Recent variants of the original GAN can be used for end-to-end, cross-domain learning between two high-dimensional domains, by appying autoencoder-like model designs, such as U-Net (Isola et al., 2017). Specifically, CycleGAN consists of two pairs of GANs ($\mathcal{G}_{X\to Y}, \mathcal{D}_Y$) and ($\mathcal{G}_{Y\to X}, \mathcal{D}_X$) (Zhu et al., 2017). Each pair of GAN is responsible for learning the mapping from one domain to the other. Thus, given (unpaired) training data sets from two domains (X and Y), the generative model $\mathcal{G}_{X\to Y}$ learns how to map a sample (x) from domain X to domain Y, whereas the generative model $\mathcal{G}_{Y\to X}$ learns how to map a sample (y) from domain Y to X. $\mathcal{D}_Y$ determines the probability of a sample (y) coming from the generator distribution $p^{\mathcal{G}_{X\to Y}}_{\text{model}}(y)$ or from the original data set $p^Y_{\text{data}}(y)$. Similarly, $\mathcal{D}_X$ gives the probability of a sample (x) coming from $p^{\mathcal{G}_{Y\to X}}_{\text{data}}(x)$ or from the original data set $p^X_{\text{data}}(x)$.

To adapt CycleGAN for 4-D seismic data analyses, we consider the forward and inverse problems in 4-D seismic as a special form of cross-domain learning. Specifically, the forward and inverse problems may be formulated by using two pairs of generative and discriminative models

$$\begin{aligned} \text{Forward process,} \quad & \mathcal{G}_{X\to Y} : \mathbb{R}_X \to \mathbb{R}_Y, \mathcal{D}_Y : \mathbb{R}_Y \to [0,1], \\ \text{Inverse process,} \quad & \mathcal{G}_{Y\to X} : \mathbb{R}_Y \to \mathbb{R}_X, \mathcal{D}_X : \mathbb{R}_X \to [0,1], \end{aligned}$$

where $\mathcal{G}_{X\to Y}$ defines a forward generative model from domain X (fluid saturation) to domain Y (rock elastic properties), while $\mathcal{G}_{Y\to X}$ defines the inverse generative model that maps the information from domain Y to domain X.

The loss function of CycleGAN includes three terms, the adversarial loss for each generator/discriminator pair (Goodfellow et al., 2014) and a cycle consistency loss (Zhu et al., 2017)

$$\mathcal{L}(\mathcal{G}_{X\to Y}, \mathcal{G}_{Y\to X}, \mathcal{D}_X, \mathcal{D}_Y) = \mathcal{L}_{GAN}(\mathcal{G}_{X\to Y}, \mathcal{D}_Y, X, Y) \tag{19}$$

$$+\mathcal{L}_{GAN}(\mathcal{G}_{Y\to X}, \mathcal{D}_X, Y, X) \tag{20}$$

$$+\mathcal{L}_{cyc}(\mathcal{G}_{X\to Y}, \mathcal{G}_{Y\to X}), \tag{21}$$

where

$$\mathcal{L}_{\text{GAN}}(\mathcal{G}_{X\to Y}, \mathcal{D}_Y, X, Y) = \mathbb{E}_{y\sim p^Y_{\text{data}}(y)}[\log \mathcal{D}_Y(y)] + \mathbb{E}_{x\sim p^X_{\text{data}}(x)}[\log(1 - \mathcal{D}_Y(\mathcal{G}_{X\to Y}(x))], \tag{22}$$

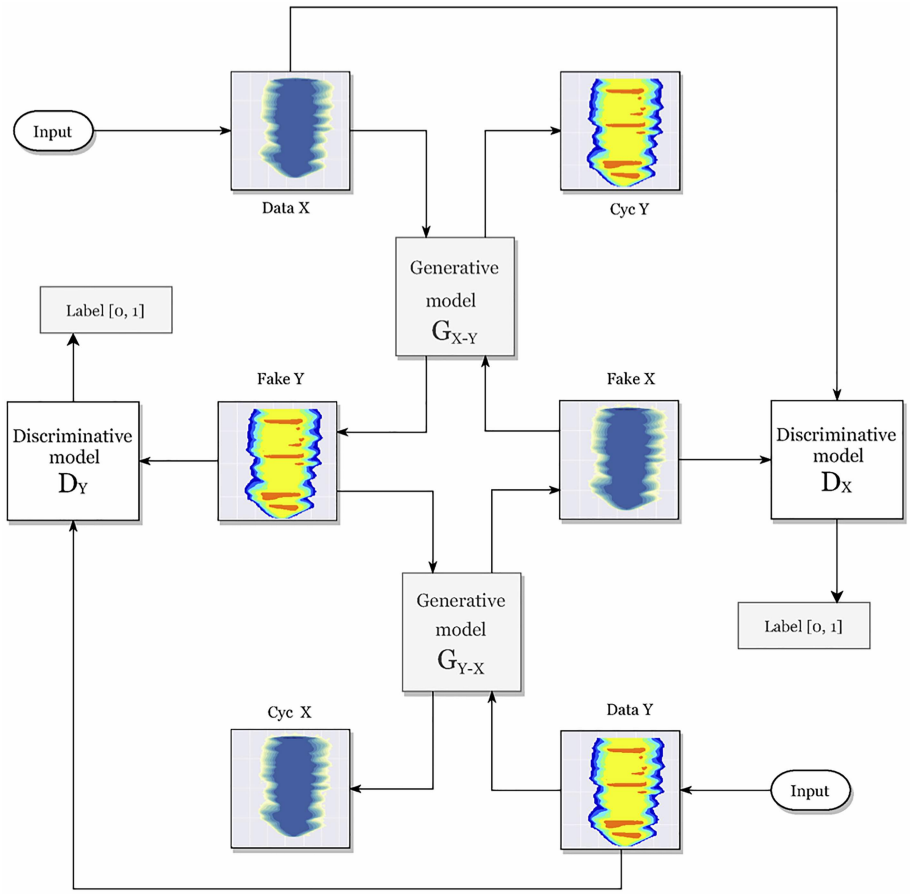

Figure 2. The workflow of CycleGAN used for solving forward and inverse problems in 4-D seismic consists of two pairs of generative and discriminative models. In the forward process, input from *DataX* is fed to the forward generative model ($\mathcal{G}_{X\to Y}$) and then outputs the predicted result (*FakeY*). Then data *FakeY* is fed to the inverse generative model ($\mathcal{G}_{Y\to X}$) to reconstruct the *DataX*, which results in *CycX*. The reconstruction loss is calculated by comparing *CycX* and *DataX*. Similarly, the inverse workflow uses samples from *DataY* to generate *FakeX* and then calculates *CycY*. The discriminative model (D_Y) is used for determining the probability of the generated *FakeY* coming from the real *DataY* distribution. The discriminative model (D_X) is used to determine the probability of generated *FakeX* belonging to real *DataX* distribution.

$$\mathcal{L}_{\text{GAN}}(\mathcal{G}_{Y\to X}, \mathcal{D}_X, Y, X) = \mathbb{E}_{x\sim p^X_{\text{data}}(x)}[\log \mathcal{D}_X(x)] + \mathbb{E}_{y\sim p^Y_{\text{data}}(y)}[\log(1-\mathcal{D}_X(\mathcal{G}_{Y\to X}(y))], \tag{23}$$

$$\mathcal{L}_{cyc}(\mathcal{G}_{X\to Y}, \mathcal{G}_{Y\to X}) = \mathbb{E}_{x\sim p^X_{\text{data}}(x)}[\left\|\mathcal{G}_{Y\to X}(\mathcal{G}_{X\to Y}(x)) - x\right\|_1] + \mathbb{E}_{y\sim p^Y_{\text{data}}(y)}[\left\|\mathcal{G}_{X\to Y}(\mathcal{G}_{Y\to X}(y)) - y\right\|_1], \tag{24}$$

where $\mathbb{E}$ is the expectation operator. The unknown GAN parameters can be obtained by solving the following minimax problem:

$$\hat{\theta}^{(\mathcal{G}_{X\to Y})}, \hat{\theta}^{(\mathcal{G}_{Y\to X})}, \hat{\theta}^{(\mathcal{D}_X)}, \hat{\theta}^{(\mathcal{D}_Y)} = \arg \min_{\theta^{(\mathcal{G}_{X\to Y})}, \theta^{(\mathcal{G}_{Y\to X})}} \max_{\theta^{(\mathcal{D}_X)}, \theta^{(\mathcal{D}_Y)}} \mathcal{L}(\mathcal{G}_{X\to Y}, \mathcal{G}_{Y\to X}, \mathcal{D}_X, \mathcal{D}_Y), \tag{25}$$

where $\hat{\theta}$ are the unknown GAN parameters.

Figure 2 shows the workflow of CycleGAN. In this work, instead of learning mappings between fluid saturation to seismic elastic properties, we learn the mappings between their changes to mitigate the impact of systematic errors and uncertain initial values. In other words, domain X corresponds to reservoir fluid property changes such as the gas saturation change (ΔS_g), for which the training data can be obtained by running the forward reservoir simulation model for given reservoir properties (e.g., permeability and porosity) and well schedule (gas injection rate). Domain Y corresponds to seismic elastic property changes, such as the AI change (ΔAI), for which the training data can be calculated based on equations (15) and (5).

For this study, CycleGAN is implemented by using deep convolutional neural networks, as shown in Zhong, Sun, and Jeong (2019) (Figure 3). Similar to the original CycleGAN design presented in Zhu et al. (2017),

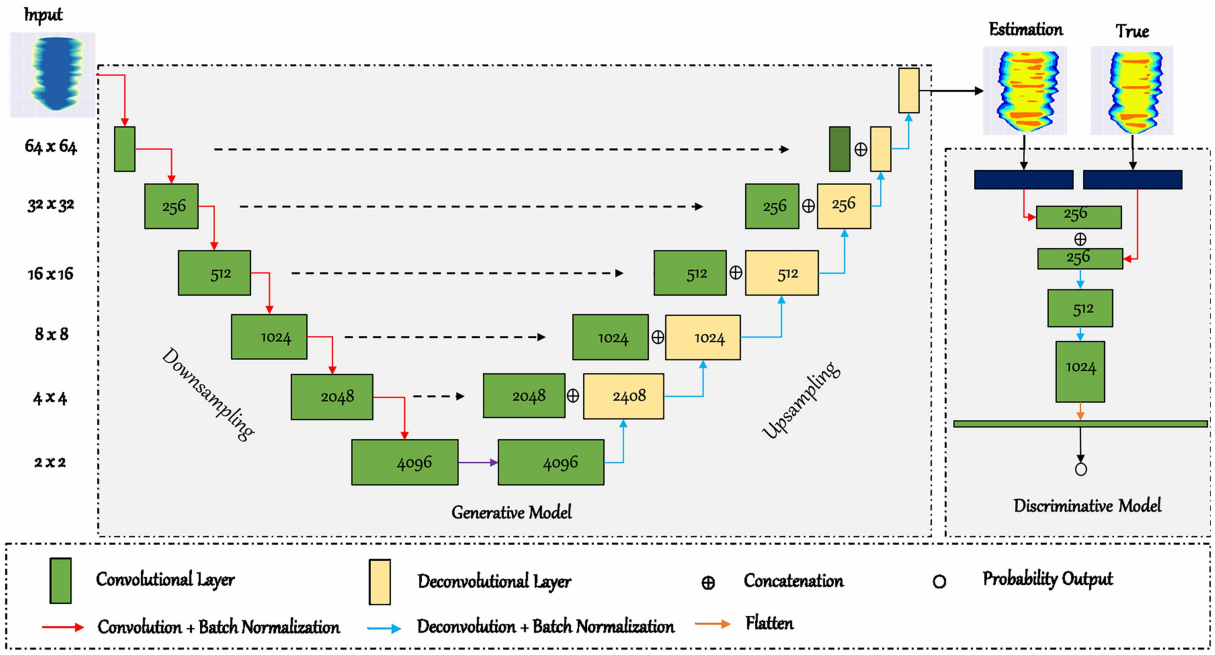

Figure 3. The topology of generative and discriminative model used in CycleGAN. Both generative models $G_{X\to Y}$ and $G_{Y\to X}$ share the same network structures, and both discriminative models D_X and D_Y share the same structures.

the two generative models share the same end-to-end deep learning neural network architecture, which includes a series of convolutional layers to extract fine-scale features from the input data, followed by a series of deconvolutional layers to learn coarse-scale features and to generate a target image that has the same sizes as the input data (i.e., 128×128). The kernel size used in the downsampling path is 4×4, and the stride size is 2. Deconvolutional layers in the upsampling path have the same kernel and stride settings. The leaky rectified linear unit function (ReLU) is used as the activation function for all hidden CNN layers, and the hyperbolic tangent function (tanh) is used as the activation function for the output layer.

2.5. Performance Metrics

Three metrics are used to quantify the performance of CycleGAN. The structural similarity index (SSIM) commonly used in image analysis (Wang et al., 2004) provides a measure of "perceptual difference" between two images. For two sliding windows $\mathbf{u}$ and $\mathbf{v}$, the SSIM is defined by

$$SSIM(\mathbf{u},\mathbf{v}) = \frac{2\mu_{\mathbf{u}}\mu_{\mathbf{v}} + C_1}{\mu_{\mathbf{u}}^2 + \mu_{\mathbf{v}}^2 + C_1} \cdot \frac{2\sigma_{\mathbf{uv}} + C_2}{\sigma_{\mathbf{u}}^2 + \sigma_{\mathbf{v}}^2 + C_2}, \tag{26}$$

where $\mu_{\mathbf{u}}$ and $\mu_{\mathbf{v}}$ are the mean values of windows $\mathbf{u}$ and $\mathbf{v}$, $\sigma_{\mathbf{u}}$ and $\sigma_{\mathbf{v}}$ are the standard deviation of windows $\mathbf{u}$ and $\mathbf{v}$, $\sigma_{\mathbf{uv}}$ is the covariance of window $\mathbf{u}$ and window $\mathbf{v}$. $C_1 = (k_1 L)^2$ where $k_1 = 0.01$ and $C_2 = (k_2 L)^2$ where $k_2 = 0.03$ and $L = 1$ (Wang et al., 2004). In this study, the sizes of sliding windows $\mathbf{u}$ and $\mathbf{v}$ are both set to 11×11 pixels (grid cells).

Root-square-mean error (RMSE) is another commonly used metric (Zhong & Carr, 2016; Zhong et al., 2018) and is defined as

$$RMSE = \sqrt{\frac{1}{N}\sum_{i=1}^{N} \|\mathbf{x}^i - \hat{\mathbf{x}}^i\|_2^2}, \tag{27}$$

where N is the number of samples and $\mathbf{x}$ and $\hat{\mathbf{x}}$ are the true and CycleGAN-generated samples (can be in either domain), respectively.

The coefficient of determination (R^2) is a metric to measure the closeness between two variables, which is defined by

$$R^2 = 1 - \frac{\sum_{i=1}^{N} (\mathbf{x}^i - \hat{\mathbf{x}}^i)^2}{\sum_{i=1}^{N} (\mathbf{x}^i - \bar{\mathbf{x}})^2}, \tag{28}$$

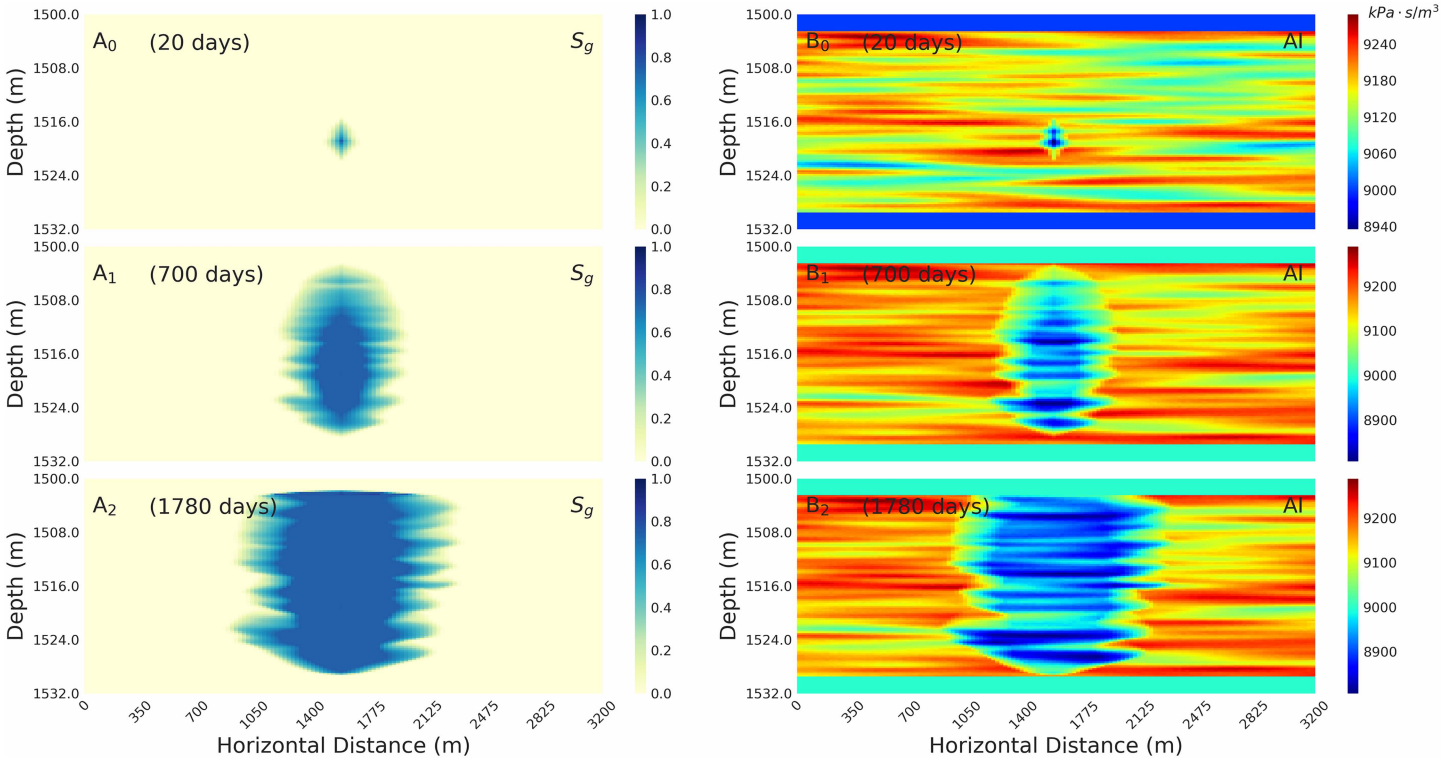

Figure 4. Gas saturation distribution (S_g) after (A_1) 20, (A_2) 700, and (A_3) 1,780 days of CO_2 injection and the corresponding acoustic impedance (AI) after (B_1) 20, (B_2) 700, and (B_3) 1,780 days of CO_2 injection for the corresponding geological model shown in Figure 1.

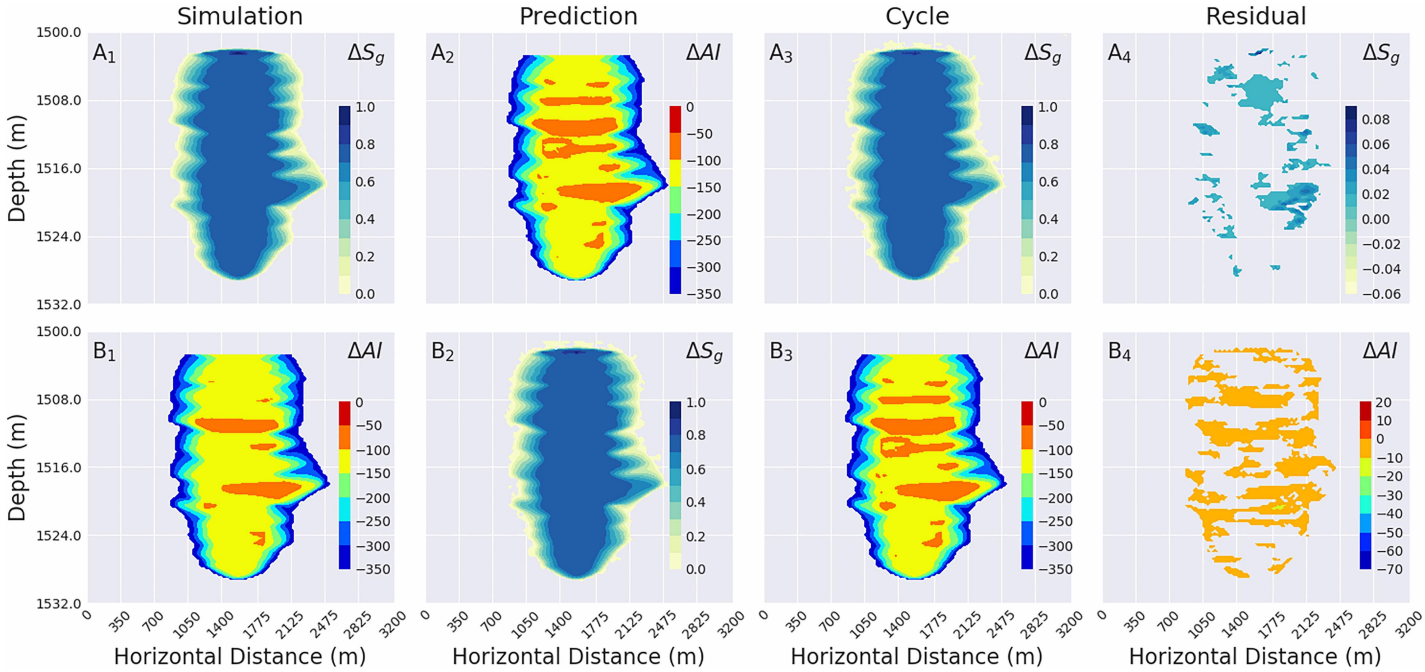

Figure 5. Illustration of the training performance of CycleGAN for a single realization used in the base case. A_1 shows the gas saturation change (ΔS_g) calculated based on CMG simulation, A_2 shows the acoustic impedance (AI) change ($\Delta\hat{AI}$) predicted by the generative model ($\mathcal{G}_{X\to Y}$), A_3 is the gas saturation change ($\Delta\hat{S}_g$) reconstructed by using generative model ($\mathcal{G}_{Y\to X}$) from the predicted AI change ($\Delta\hat{AI}$), A_4 shows the difference between A_1 and A_3. Same as Figure 5(A); B_1 is the calculated AI change (ΔAI) by using the rock physics model, B_2 shows the gas saturation change ($\Delta\hat{S}_g$) predicted by the generative model ($\mathcal{G}_{Y\to X}$) from ΔAI, B_3 shows the AI change ($\Delta\hat{AI}$) reconstructed by using the generative model ($\mathcal{G}_{X\to Y}$) from the predicted $\Delta\hat{S}_g$, and B_4 shows the difference between B_1 and B_3.

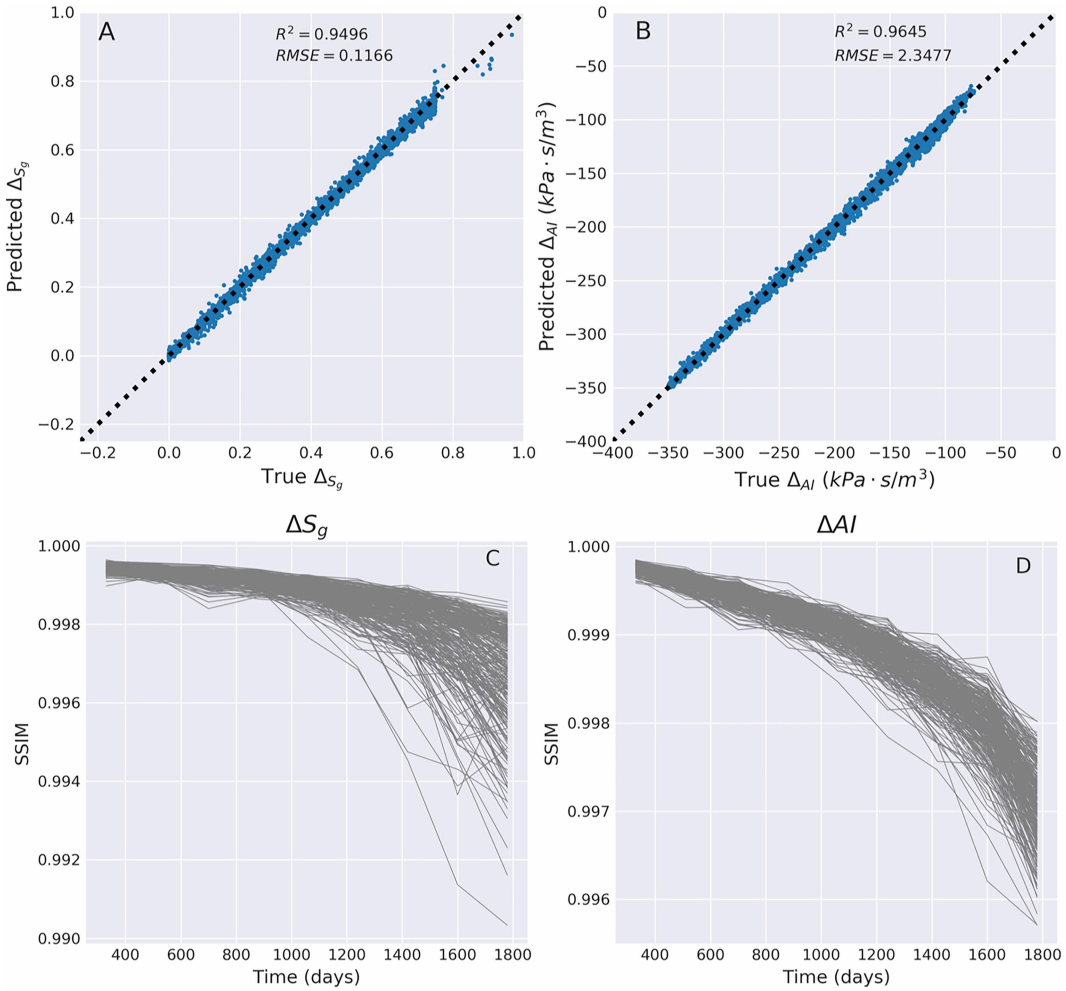

Figure 6. (a) Scatter plot of CO_2 saturation change generated by CMG-GEM, ΔS_g, and that by the inverse generative model $\mathcal{G}_{Y \to X}(\Delta AI)$, $\Delta \hat{S}_g$. (b) Scatter plot of acoustic impedance change calculated based on rock physics model (ΔAI) and by the forward generative model $\mathcal{G}_{Y \to X}(\Delta S_g)$, $\Delta \hat{AI}$. (c) Plots of SSIM values obtained on the training ensemble of 225 realizations for ΔS_g. (d) Plots of SSIM values obtained on the training ensemble of 225 realizations for ΔAI.

where N is the number of samples, $\mathbf{x}^i$ and $\mathbf{x}^i$ are the true and CycleGAN-generated samples, respectively, and $\bar{\mathbf{x}}$ is the average value of the true image.

3. Results and Discussion

3.1. Creation of the Synthetic Data Set

We use CMG-GEM to solve the multiphase flow problem described in section 2.2. The injection well is located in the center of the reservoir (block square in Figure 1). The maximum time step in solving equation (2) is set to 2.5 days. A much larger time step (0.5 years) is used to update the rock elastic properties through the RPM described under section 2.3. A total of 300 forward simulations is run for different stochastic realizations of permeability/porosity, from which the CO_2 saturation (S_g), water saturation (S_w), and reservoir pressure (P) are saved at the monthly interval. Figure 4a shows the CO_2 distribution after 20, 700, and 1,780 days of CO_2 injection for the corresponding geological model shown in Figure 1. It can be seen that the spatial distribution of CO_2 saturation is not symmetric because of heterogeneity in reservoir properties. Overall, the CO_2 plume tends to migrate in the lateral direction (note that the vertical/horizontal scale ratio is 1:100 for visualization purposes). In this case, the horizontal fingering of CO_2 plume makes the prediction of acoustic impedance (AI) a challenging problem.

According to equation (5), we can calculate the reservoir rock density at any time instance once the reservoir fluid saturation is available. Then the P wave velocity (V_p) can be calculated based on the RPMs (i.e.,

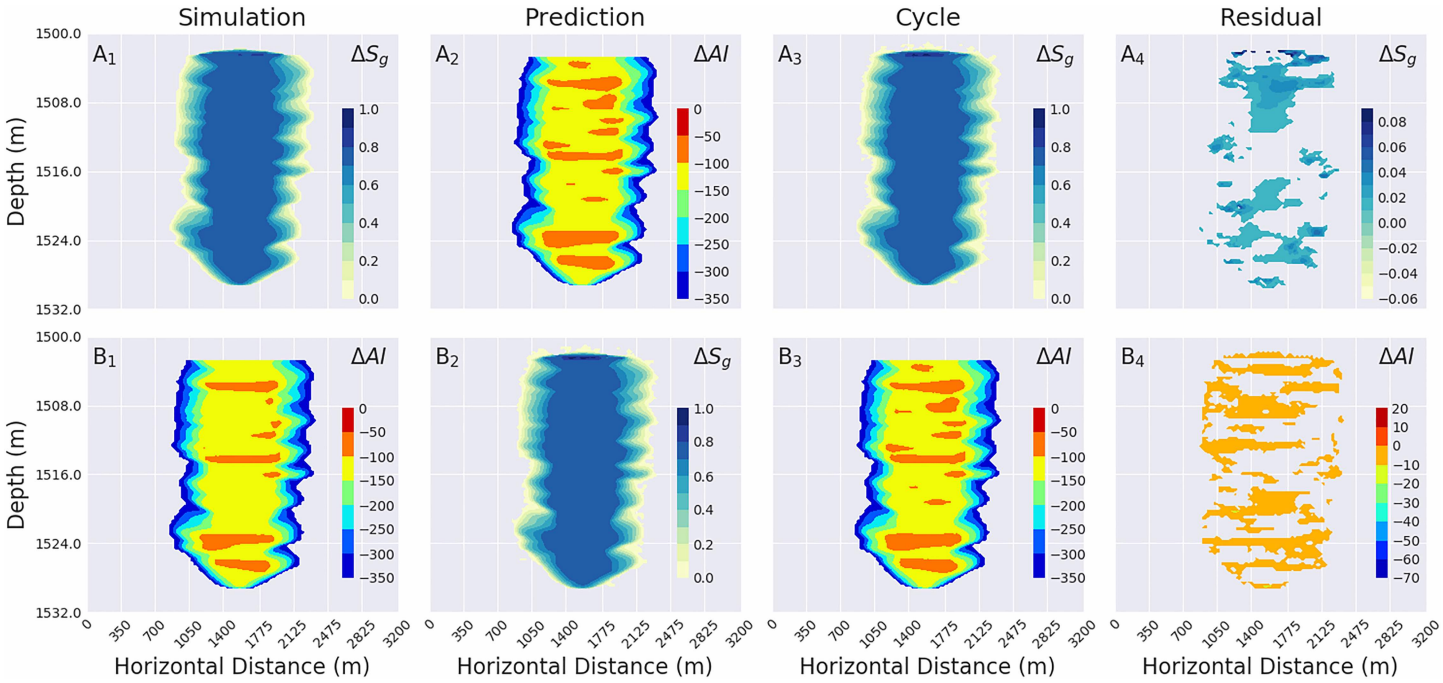

Figure 7. Illustration of the testing performance of CycleGAN on a single permeability realization in the base case. A_1 shows the gas saturation change (ΔS_g) calculated based on CMG simulation, A_2 shows the elastic property change ($\Delta\hat{AI}$) predicted by the forward generative model ($G_{X\to Y}$), A_3 is the gas saturation change ($\Delta\hat{S}_g$) reconstructed by using the inverse generative model ($G_{Y\to X}$) from the predicted elastic property change ($\Delta\hat{AI}$), A_4 shows the difference between A_1 and A_3. Same as Figure 5a; B_1 is the elastic property change (ΔAI) calculated by using the rock physics model, B_2 shows the gas saturation change ($\Delta\hat{S}_g$) predicted by the inverse generative model ($G_{Y\to X}$) from ΔAI, B_3 shows the elastic property change ($\Delta\hat{AI}$) reconstructed by the generative model ($G_{X\to Y}$) from the predicted $\Delta\hat{S}_g$, and B_4 shows the difference between B_1 and B_3.

equations (12) and (15)) after the bulk density of the reservoir is calculated. In this workflow, the bulk density and P wave velocity are the intermediate parameters, which are used to calculate AI

$$AI = V_P \cdot \rho_b, \quad (kPa \cdot s/m^3) \tag{29}$$

where V_P is the P wave velocity and ρ_b is the bulk density. Figure 4b shows the AI at 20, 700, and 1,780 days that correspond to fluid saturations in Figure 4a.

As mentioned before, instead of learning the mappings between actual values (i.e., the actual gas saturation S_g and AI), we train the CycleGAN model to learn the time-lapse changes of these variables (i.e., ΔS_g and ΔAI), which are defined by the following formulae,

$$\Delta S_g^t = S_g^t - S_g^0 \tag{30}$$

$$\Delta AI^t = AI^t - AI^0 \tag{31}$$

where ΔS_g^t is the change in gas saturation at time t relative to its initial value (S_g^0) and ΔAI^t is the change in AI at time t relative to its initial value (AI^0). The main advantage of this approach is that we do not need to know the actual AI values to predict the gas saturation, thus avoiding the impact of uncertain initial conditions and potential systematic errors.

3.2. Training and Testing Performance

Here we analyze the training performance of CycleGAN and investigate its capability for reservoir property change inversion using the synthetic data set described in the previous subsection. We use the simulation results from 225 permeability realizations (i.e., 75% of the total of 300 realizations) to train the CycleGAN and the simulation results from the remaining 75 permeability realizations for testing. This split ensures that there is no overlap between any of the training and testing samples.

Figure 5a compares the simulated CO_2 saturation changes (ΔS_g) and CycleGAN predicted CO_2 saturation changes ($\Delta\hat{S}_g$) for the training data set at 1,780 days. Specifically, Figure 5a1 shows the CMG-GEM simulated CO_2 saturation changes (ΔS_g), and Figure 5a2 shows the CycleGAN estimated AI changes ($\Delta\hat{AI}$)

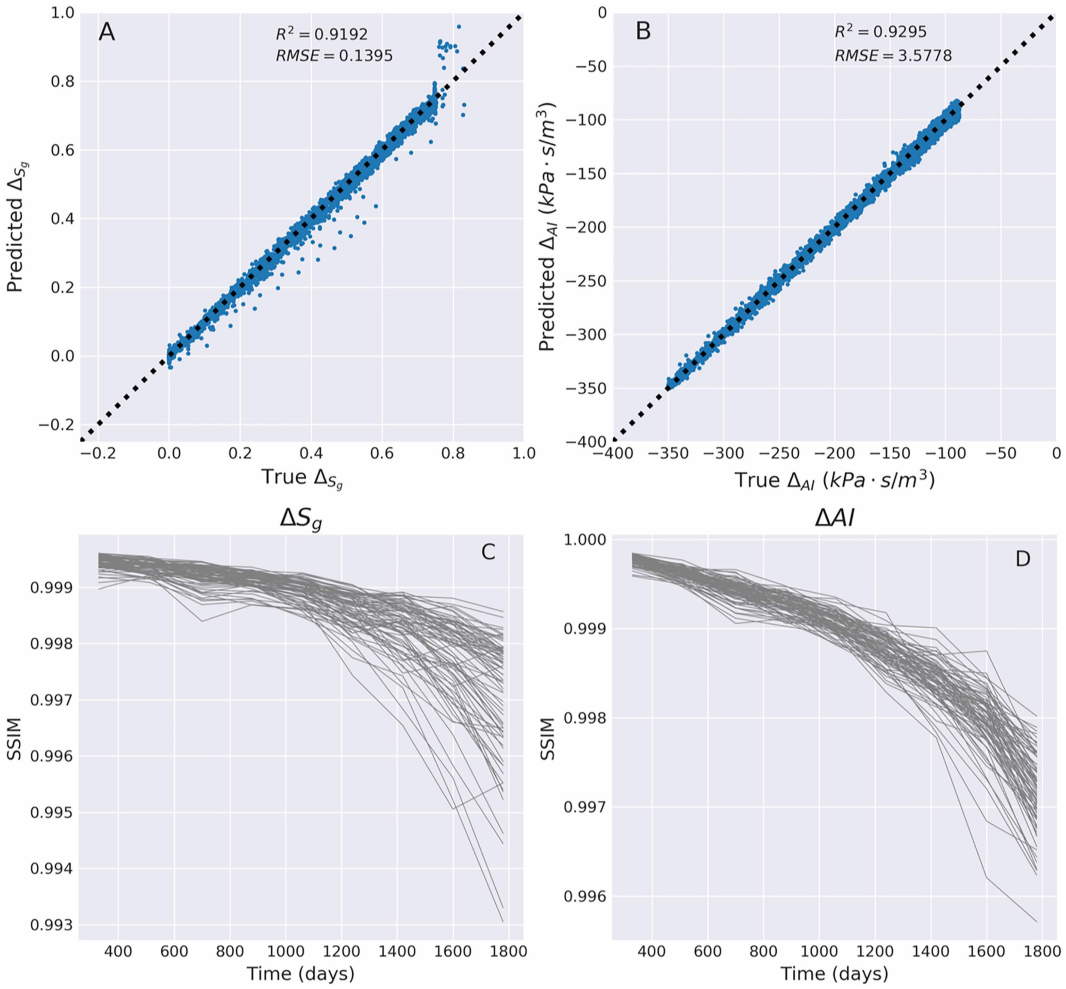

Figure 8. (a) Comparison of CMG simulation-based CO_2 saturation changes (ΔS_g) and CO_2 saturation changes ($\Delta \hat{S}_g$) generated by inverse generative model ($\mathcal{G}_{Y \to X}$). (b) Acoustic impedance (AI) change (ΔAI) calculated based on rock physics model and AI changes ($\Delta \hat{AI}$) reconstructed by CycleGAN ($\mathcal{G}_{X \to Y}$). (c) Plots of SSIM values obtained on the testing ensemble of 75 realizations for ΔS_g. (d) Plots of SSIM values obtained on the testing ensemble of 75 realizations for ΔAI.

from ΔS_g (i.e., using the forward mapping $\mathcal{G}_{X \to Y}(\Delta S_g)$). Figure 5a3 shows the CycleGAN estimated CO_2 saturation changes ($\Delta \hat{S}_g$) at 1,780 days using the inverse mapping $\mathcal{G}_{Y \to X}(\Delta AI)$), and Figure 5a4 shows the difference between Figures 5a1 and 5a3. In this case, the presence of CO_2 plume lowers the effective density and the *P* wave velocity, leading to reduced AI inside the plume (Figure 5b1). In the second row of Figure 5, Figure 5b displays the comparison between RPM calculated and CycleGAN estimated AI change ($\Delta \hat{AI}$) for the training data set at time instance of 1,780 days. In particular, Figure 5b1 illustrates the RPM calculated ΔAI, Figure 5b2 shows the CycleGAN predicted $\Delta \hat{S}_g$ from ΔAI (using the inverse mapping $\mathcal{G}_{Y \to X}(\Delta AI)$), and Figure 5b3 shows the reconstructed $\Delta \hat{AI}$ from $\Delta \hat{S}_g$ (using the forward mapping $\mathcal{G}_{X \to Y}(\Delta \hat{S}_g)$). Figure 5b4 displays the residual between Figures 5b1 and 5b3. It can be seen that the generative model ($\mathcal{G}_{Y \to X}$) can accurately predict the fluid saturation change based on the AI change (ΔAI), while at the same time the generative model ($\mathcal{G}_{X \to Y}$) can also estimate the AI change (ΔAI) based on the fluid saturation changes (ΔS_g) with high accuracy.

Figure 6a shows that the training saturation change (ΔS_g) and predicted saturation change ($\Delta \hat{S}_g$) have a coefficient of determination $R^2 = 0.9496$ and an *RMSE* of 0.1166. In the case of AI, Figure 6b shows that the RPM-based AI changes (ΔAI) and CycleGAN predicted AI changes ($\Delta \hat{AI}$) have a good match, with $R^2 = 0.9645$ and $RMSE = 2.3477$ ($kPa \cdot s/m^3$). Figure 6c shows the SSIM value obtained on the training ensemble of 225 realizations for ΔS_g, and Figure 6d shows the SSIM values obtained on the training ensemble

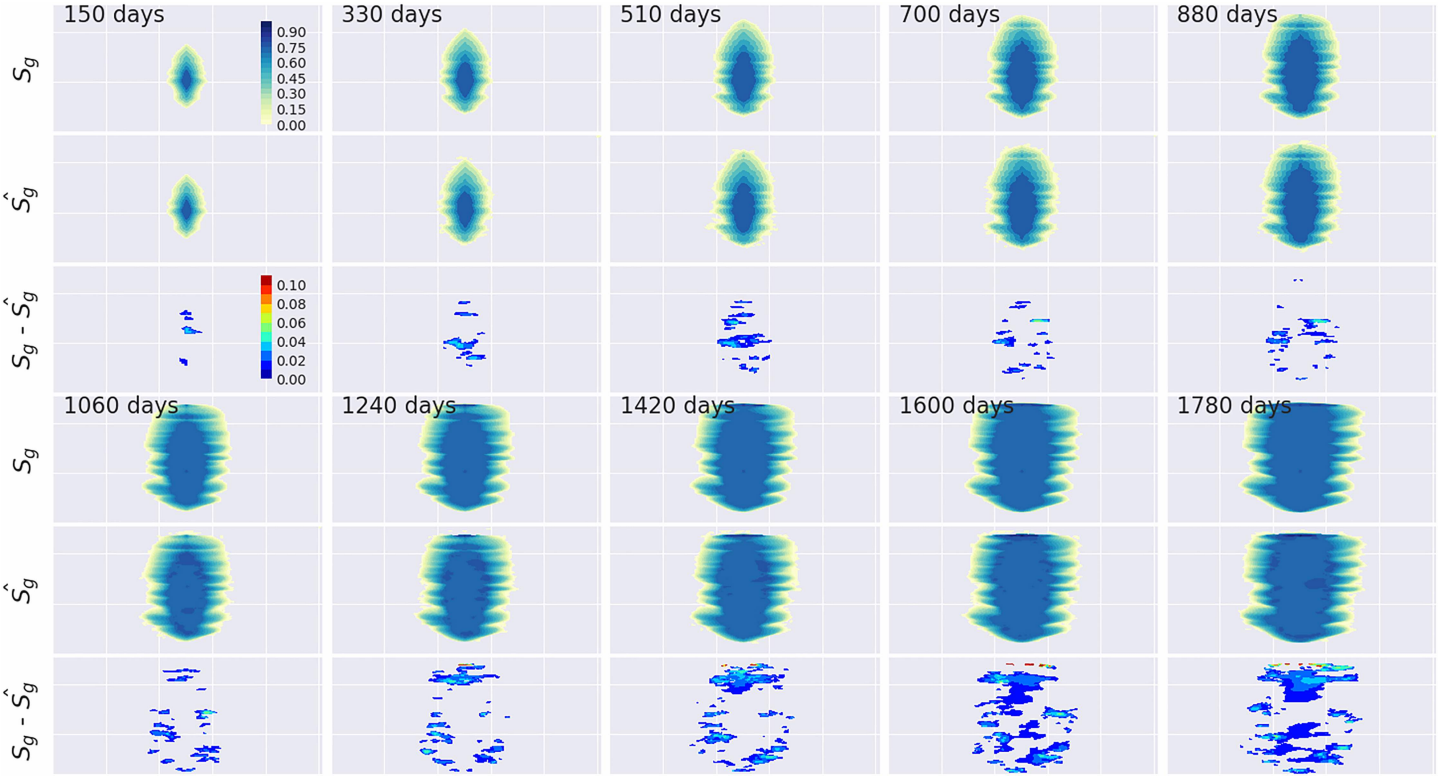

Figure 9. Snapshots of CO_2 saturation changes (ΔS_g) obtained by numerical simulation and CycleGAN model for one realization in the testing data set. Top row for each panel: CO_2 saturation changes (ΔS_g) calculated based on the numerical simulation result. Middle row for each panel: CO_2 saturation changes ($\Delta \hat{S}_g$) estimated by CycleGAN model (from inverse mapping ($G_{Y\to X}$)). Bottom row of each panel: residual error maps between each pair of maps ($\Delta S_g - \Delta \hat{S}_g$).

of 225 realizations for ΔAI. The higher the SSIM value is, the closer the two images are. Thus, Figures 5 and 6 indicate that the CycleGAN learns the statistical mappings between the training samples well.

To verify the generalization ability of the trained CycleGAN model, the CO_2 saturation changes (ΔS_g) from the testing data set, which are not used for training the CycleGAN, are fed to the forward generative model ($G_{X\to Y}$) to generate AI changes ($\Delta \hat{AI}$), and the inverse generative model ($G_{Y\to X}$) is used to estimate CO_2 saturation changes ($\Delta \hat{S}_g$) by using simulated AI changes (ΔAI). Figures 7a1 and 7a3 show the CMG-GEM simulated and CycleGAN reconstructed CO_2 saturation changes, respectively. Figure 7a4 shows the residual error between Figures 7a1 and 7a3. It can be concluded that the trained inverse generative model ($G_{Y\to X}$) can predict the fluid saturation changes with relatively low error, with $R^2 = 0.9192$ and $RMSE = 0.1395$ (Figure 8a). Similarly, the forward generative model ($G_{X\to Y}$), which uses CO_2 saturation change (ΔS_g) as input (Figure 7b1) to predict AI changes ($\Delta \hat{AI}$) (Figure 7b3), has low residual error (Figure 7b4), with $R^2 = 0.9295$ and $RMSE = 3.5778$ kPa·s/m^3 on testing data (Figure 8b). Figure 8c shows the SSIM value obtained on the testing ensemble of 75 realizations for ΔS_g, and Figure 8d shows the SSIM values obtained on the testing ensemble of 75 realizations for ΔAI. In general, we observe similar temporal patterns as seen on the training data set (Figures 6c and 6d). The ensemble of SSIM curves tends to spread with time but stays above 0.99. Thus, CycleGAN achieves a good performance on both the training and testing data.

To illustrate the temporal performance of CycleGAN, Figure 9 compares the simulated and predicted CO_2 gas saturation changes and AI changes at different times. In particular, Figure 9 shows the CMG-simulated CO_2 saturation changes (ΔS_g) for the geological model shown in Figure 1. In Figure 9, the first row shows ΔS_g, the second row shows the CycleGAN reconstructed CO_2 saturation changes ($\Delta \hat{S}_g$), and the third row shows the difference between ΔS_g and $\Delta \hat{S}_g$. It can be seen from Figure 9 that with increasing injection time, the CO_2 plume mainly spreads along the horizontal direction. At large times, the error difference between the simulation-based gas saturation changes (ΔS_g) and our proposed CycleGAN reconstructed gas saturation changes ($\Delta \hat{S}_g$) increases, but the maximum error is still capped under 0.1 and is around 0.02 in most regions. The errors mainly concentrate near the plume edges.

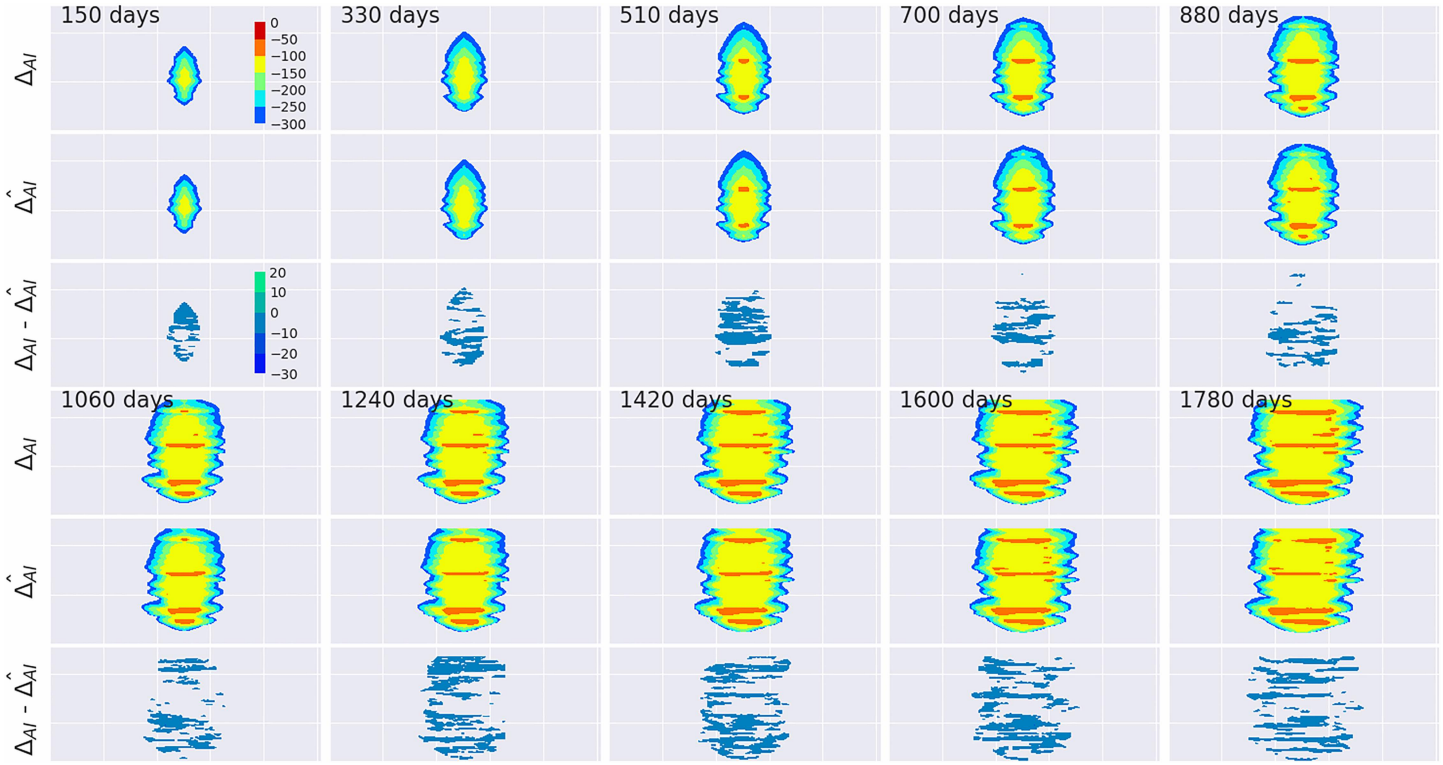

Figure 10. Snapshots of acoustic impedance changes (ΔAI) obtained by RPMs and CycleGAN model for one realization in the testing data set. Top row of each panel: acoustic impedance changes (ΔAI) calculated based on the RPMs. Middle row of each panel: acoustic impedance changes (ΔAI) estimated by CycleGAN model (from forward mapping ($G_{X\to Y}$)). Bottom row of each panel: residual error maps between each pair of maps ($\Delta AI - \Delta\hat{AI}$).

Figure 10 compares RPM-based AI changes (ΔAI) and CycleGAN predicted AI changes ($\Delta\hat{AI}$) at different times. Because the AI for each time instance is calculated based on the deterministic RPM, AI and fluid saturation share the same geometric shapes, as determined by V_P and ρ_b which, in turn, are related to reservoir permeability distribution. The first row of Figure 10 shows the RPM-based AI changes (ΔAI), the second row shows our proposed CycleGAN predicted AI changes ($\Delta\hat{AI}$), and the third row shows the difference between the two. It can be seen that the difference in AI changes, ($\Delta AI - \Delta\hat{AI}$), is in the range of [−30, 20], which is less than 10% of the maximum absolute ΔAI value of 300. Most of those errors are in the (−10,0) range. Again, Figures 9 and 10 indicate that our proposed CycleGAN not only can predict the AI changes ($\Delta\hat{AI}$) from fluid saturation changes (ΔS_g) well (i.e., the forward process) but also can estimate the fluid saturation changes ($\hat{S}_g$) from ΔAI with low error (i.e., the inversion process).

Once the AI change (ΔAI) is estimated, the actual AI may be reconstructed from the following relationship if necessary,

$$AI^t = \Delta AI^t + AI^0. \tag{32}$$

By using the reconstructed AI calculated from the above equation, we can generate the seismic data (Figure 11) at different times by applying the seismic model (see supporting information). The source (wavelet s) used in the seismic model is shown in Figure 12, which is a Ricker wavelet. In general, the source is obtained using the smooth part of the amplitude spectrum of the seismic data. The first row of Figure 11 shows the actual seismic amplitude calculated based on the seismic model by applying the simulated AI (Figure 10), and the second row of Figure 11 shows the actual seismic amplitude calculated based on the seismic model by applying the predicted AI ($\hat{AI}$) (Figure 10). The third row of Figure 11 shows the seismic amplitude changes (ΔAmplitude) between seismic amplitude (first row of Figure 11) at time instances of 150 and 1,780 days, relative to the initial seismic survey (time instance of 0). The fourth row of Figure 11 shows the seismic amplitude changes (ΔAmplitude) of seismic amplitude (second row of Figure 11) at time instances of 150 and 1,780 days relative to the initial seismic survey. It can be observed that the change of

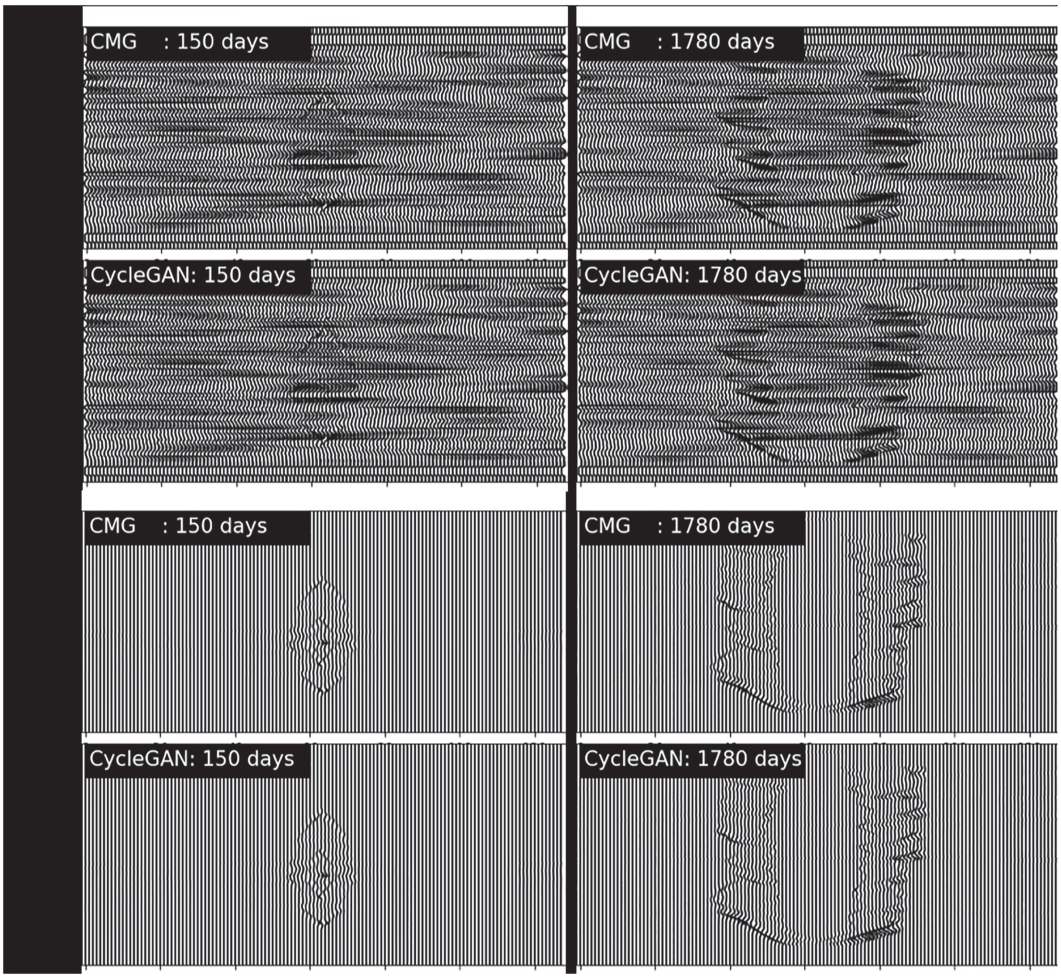

Figure 11. Comparison of seismic amplitude calculated by the seismic model based on the simulation result and CycleGAN reconstructed result. Top two rows show the actual seismic amplitude at the time instance of 150 and 1,780 days (along the depth of the reservoir); bottom two rows show the seismic amplitude changes at 150 and 1,780 days relative to time instance 0. Detailed information of seismic amplitude and its changes can be found in the supporting information (Movie S1).

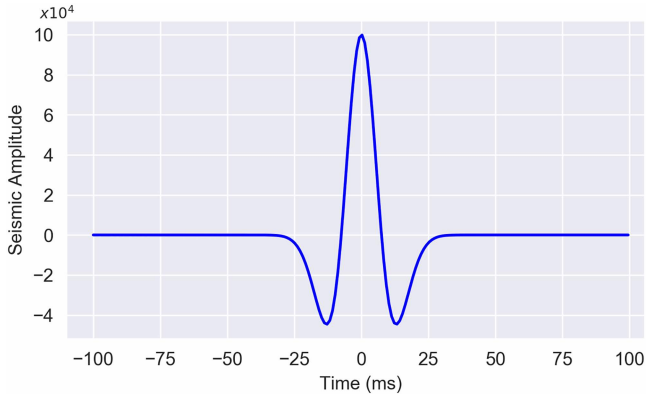

Figure 12. The wavelet *s* used in the inverse process, which is a Ricker wavelet, with a wavelength of 0.2 m, sampling rate of 1000 Hz, and pick frequency of 30 Hz. Note that all of the cases involved in this study use the same Ricker wavelet.

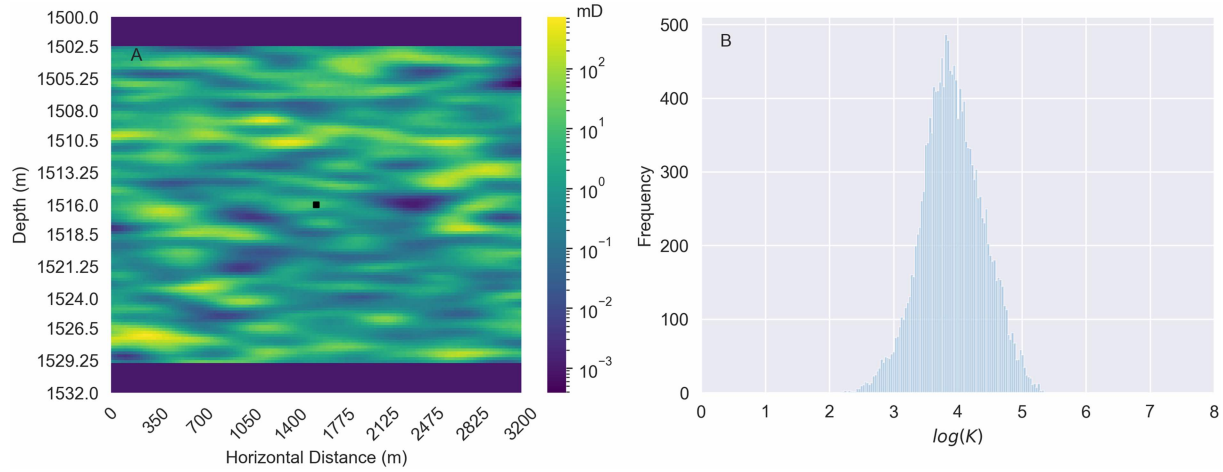

Figure 13. (a) A sample stochastic permeability field used in Case 1 (smaller correlation range). (b) Histogram of the permeability field. Note that the upper and lower sections of the reservoir are excluded when calculating the permeability histogram, and the black square shows the location of injection well.

the fluid saturation (ΔS_g in Figure 9) corresponds to the change of seismic amplitude (Figure 11). Once the change of the seismic amplitude (Figure 11) is available from, for example, time-lapse 2-D or 3-D seismic data, the fluid saturation changes can be inverted immediately. More details on the dynamic change of seismic amplitude with time can be found in the supporting information (Movie S1). Moreover, wavelet plays an important role in the seismic model, which will be discussed in section 4.

3.3. Case 1: Impact of Correlation Range

In the base case, we applied a correlation range to generate the log-permeability realization (50 grid blocks). To demonstrate the generalization ability of our proposed CycleGAN for more heterogeneous reservoirs,

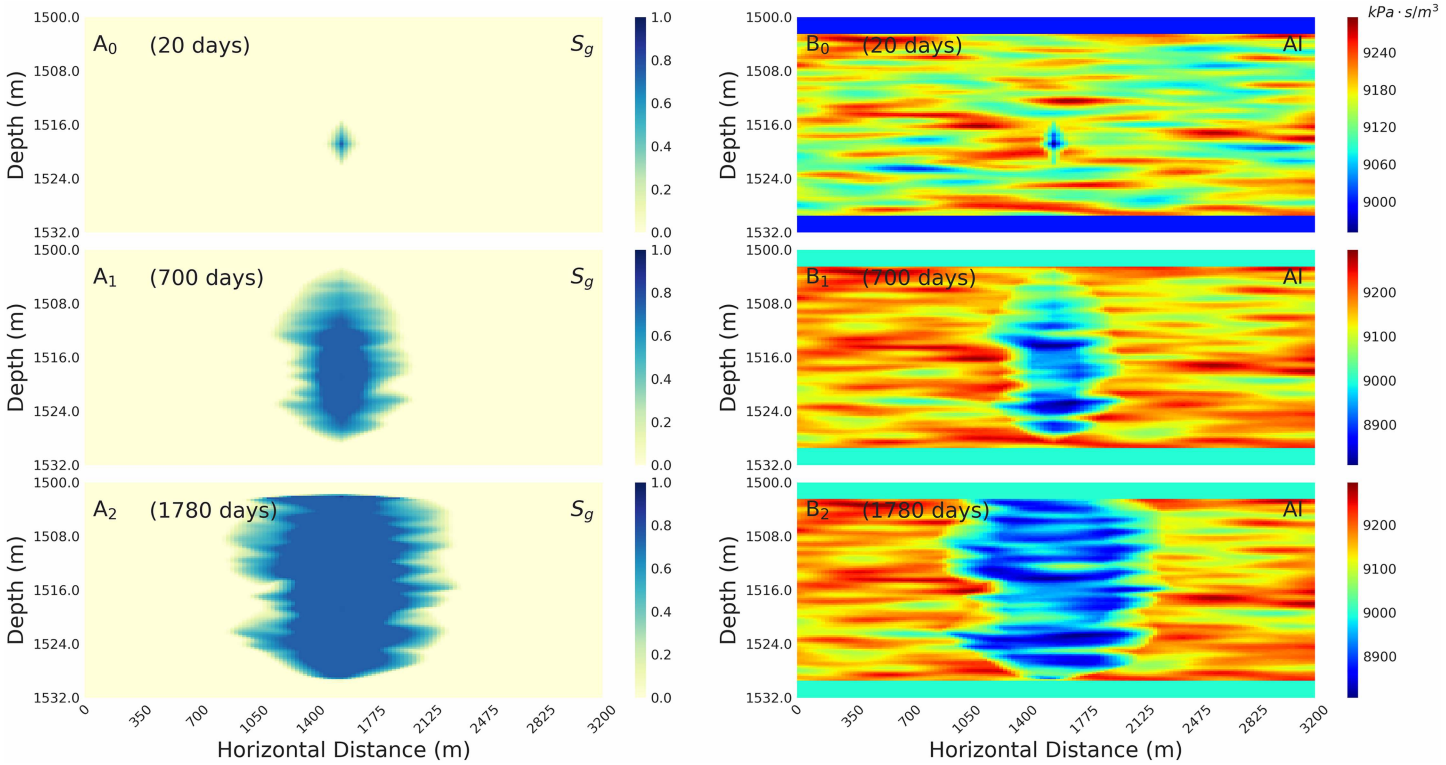

Figure 14. Gas saturation distribution (S_g) after (A_0) 20, (A_1) 700, and (A_2) 1,780 days of CO_2 injection and the corresponding acoustic impedance (AI) after (B_0) 20, (B_1) 700, and (B_2) 1,780 days of CO_2 injection for the corresponding geological model shown in Figure 13.

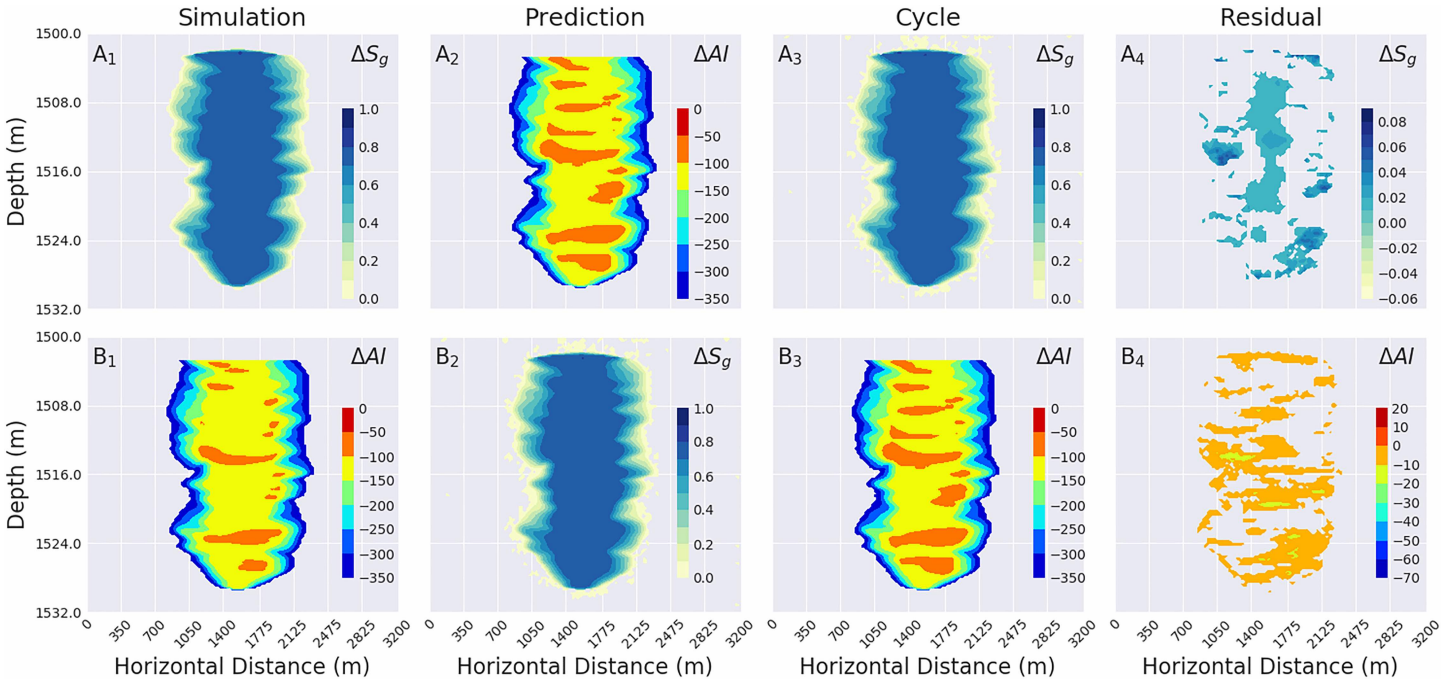

Figure 15. Illustration of testing performance of CycleGAN for one realization used in Case 1. A_1 shows the gas saturation change (ΔS_g) calculated based on CMG simulation, A_2 shows the acoustic impedance (AI) change ($\Delta\hat{AI}$) predicted by the generative model ($\mathcal{G}_{X\to Y}$), A_3 is the gas saturation change ($\Delta\hat{S}_g$) reconstructed by using the generative model ($\mathcal{G}_{Y\to X}$) from predicted AI change ($\Delta\hat{AI}$), and A_4 shows the difference between A_1 and A_3. Same as Figure 5a; B_1 is the calculated AI change (ΔAI) by using the rock physics models, B_2 shows the gas saturation change ($\Delta\hat{S}_g$) predicted by the generative model ($\mathcal{G}_{Y\to X}$) from ΔAI, B_3 shows the AI change ($\Delta\hat{AI}$), which is reconstructed by the generative model ($\mathcal{G}_{X\to Y}$) from predicted $\Delta\hat{S}_g$, and B_4 shows the difference between B_1 and B_3.

we decrease the correlation range from 50 grid blocks (in major direction) to 25 grid blocks while keeping all other parameters of the fluid model fixed. Decreasing the correlation range of the permeability model effectively increases its spatial heterogeneity. Figure 13a shows one example of the generated permeability field, and Figure 13b shows its histogram. Compared with the base case (Figure 1), the new permeability filed shows more small-scale spatial structures in the horizontal direction. Same as for the base case, 225 realizations of the geological models are simulated, and the corresponding fluid saturation changes (ΔS_g) and calculated elastic property changes (ΔAI) are collected and treated as the input and output to train the CycleGAN. As Figure 14a shows, the shape of CO_2 saturation (S_g) plume becomes more complex at various time instances than the base case (4a). Figure 14b shows the AI calculated based on the RPMs, which is also more complex than the base case (4B).

After repeating the same training process as done for the base model, the new CycleGAN model is used to predict the AI changes (ΔAI) and the gas saturation changes (ΔS_g). Figure 15a compares the simulated gas saturation changes (ΔS_g) and the CycleGAN predicted saturation changes ($\Delta\hat{S}_g$) obtained by using the inverse generative model ($\mathcal{G}_{Y\to X}$) at 1,780 days, and Figure 15b shows the comparison between RPM-based AI changes (ΔAI) and the CycleGAN predicted AI changes ($\Delta\hat{AI}$) obtained by using the forward mapping ($\mathcal{G}_{X\to Y}$) at 1,780 days. It can be seen that the inverse generative model ($\mathcal{G}_{Y\to X}$) can accurately predict ΔS_g based on the AI change (ΔAI), meanwhile the forward generative model ($\mathcal{G}_{X\to Y}$) can also estimate ΔAI based on ΔS_g with high accuracy. As Figure 16 shows, the trained inverse generative model ($\mathcal{G}_{Y\to X}$) can predict the fluid saturation changes with low error, with a R^2 of 0.9114 and *RMSE* of 0.1482 (Figure 16a). Same as the inverse generative model ($\mathcal{G}_{Y\to X}$), the forward generative model ($\mathcal{G}_{X\to Y}$), which uses the CO_2 saturation change (ΔS_g) as input, generates AI changes ($\Delta\hat{AI}$) with relatively low error ($R^2 = 0.9091$ and $RMSE = 4.3883$ kPa·s/m^3) (Figure 16b). Figures 16c and 16d show the SSIM value calculated between true ΔS_g and ΔAI and CycleGAN predicted $\Delta\hat{S}_g$ and $\Delta\hat{AI}$, respectively. As Table 3 listed, when the correlation range is reduced (from Base case to Case 1), the performance metrics (R^2 and *RMSE*) of CycleGAN are little affected for the ΔS_g prediction. The *RMSE* of CycleGAN for the ΔAI prediction increases by about 0.81 kPa·s/m^3, which is still small compared to the max value of the AI. Figure S1 shows the seismic amplitude at different

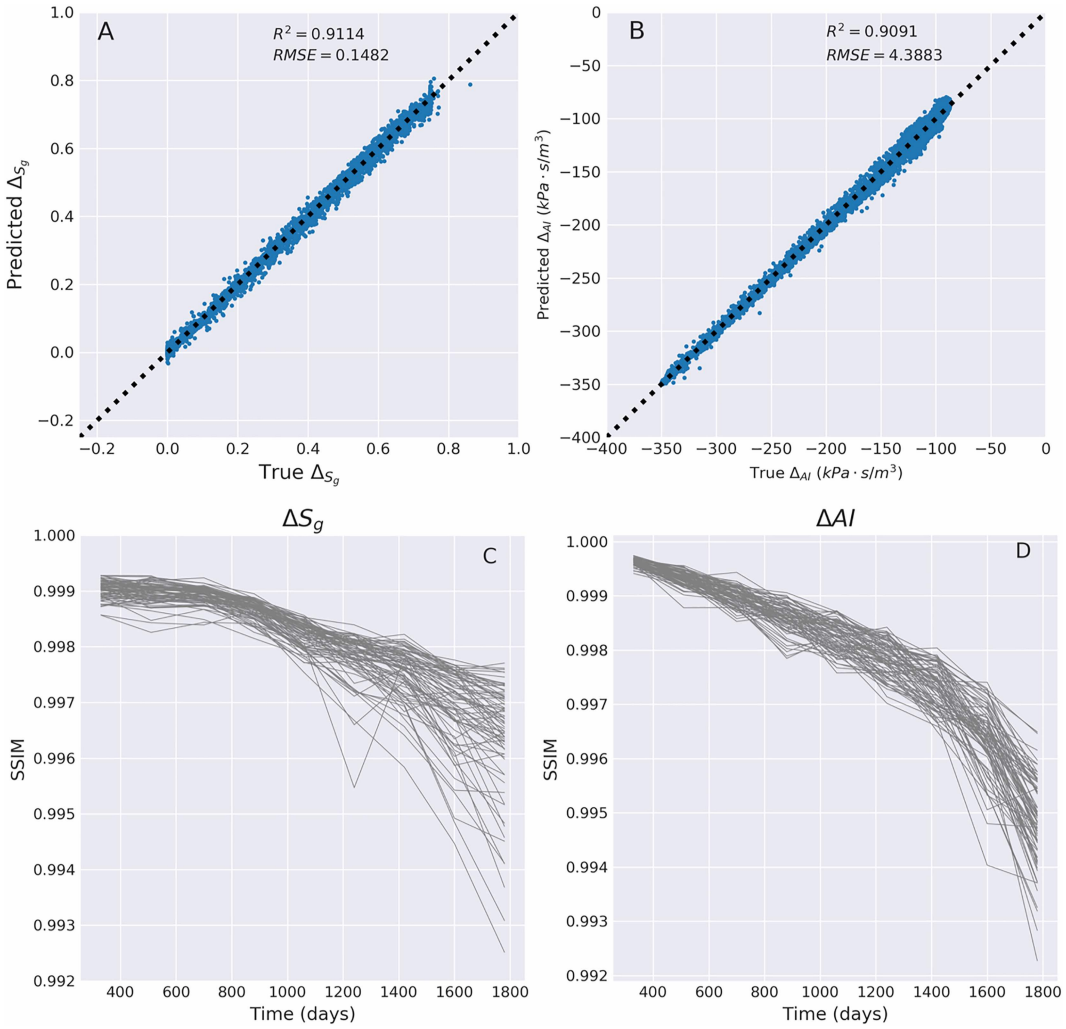

Figure 16. (a) Comparison of CMG simulation-based CO_2 saturation changes (ΔS_g) and CO_2 saturation changes ($\Delta \hat{S}_g$) generated by the generative model ($G_{X\to Y}$) for Case 1. (b) Acoustic impedance change (ΔAI) calculated based on rock physics model and AI changes ($\Delta \hat{AI}$) reconstructed by CycleGAN ($G_{X\to Y}$). (c) Plots of SSIM values obtained on the testing ensemble of 75 realizations for ΔS_g. (d) Plots of SSIM values obtained on the testing ensemble of 75 realizations for ΔAI.

time steps by using seismic model after AI are reconstructed by applying equation (32). As Figure S1 shows, the difference between simulation-based seismic amplitude and CycleGAN predicted seismic amplitude is small.

3.4. Case 2: Impact of Standard Deviation

To investigate the effect of higher spatial variability on the performance of CycleGAN, we increase the standard deviation (σ_k) of $\log k$ from 0.5 to 1.0, while all other parameters are the same as those in the base case. One realization of permeability distribution used in Case 2 is shown in Figure 17a, and the corresponding

Table 3
Performance Matrix of Testing Realization for Different Scenarios

			ΔAI		ΔS_g	
Case #	Correlation range (blocks)	Std dev	R^2	$RMSE$ (kPa·s/m^3)	R^2	$RMSE$ (—)
Base	50	0.5	0.9295	3.5778	0.9192	0.1395
Case1	25	0.5	0.9091	4.3883	0.9114	0.1482
Case2	50	1	0.9284	5.6720	0.9046	0.1650

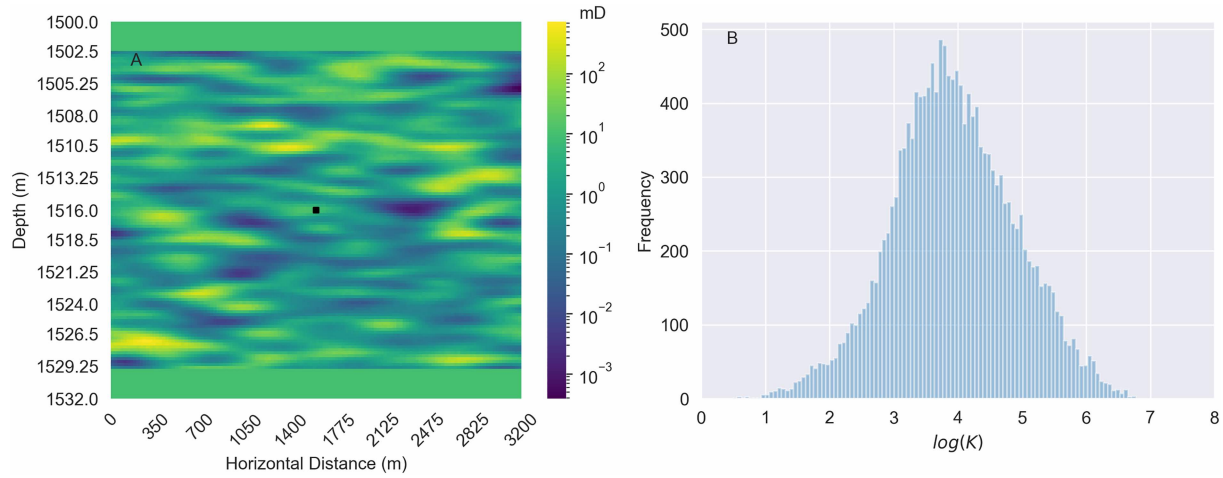

Figure 17. (a) A sample stochastic permeability field of the synthetic 2-D geological reservoir model used in Case 2 (large variability). (b) Histogram of the permeability field. Note that the upper and lower sections of the reservoir are excluded when calculating the permeability histogram, and the black dot shows the location of injection well.

histogram is shown in Figure 17b. Same as in the base case, 225 simulations, which are obtained by running CMG-GEM, are used to train the new CycleGAN, and the remaining 75 simulations are used to test the performance of the trained CycleGAN. Figure S2 shows the actual gas saturation distribution (S_g) and AI at time instances of 20, 700, and 1,780 days for the geological model given in Figure 17.

Figure 18 shows the comparison of simulation and prediction results for a single realization. Figure 19a displays the scatter plot between the true ΔS_g and CycleGAN predicted $\Delta \hat{S}_g$, and Figure 19b shows the scatter plot between RPM calculated ΔAI and CycleGAN predicted $\Delta \hat{AI}$. The forward generative model ($G_{X\to Y}$)

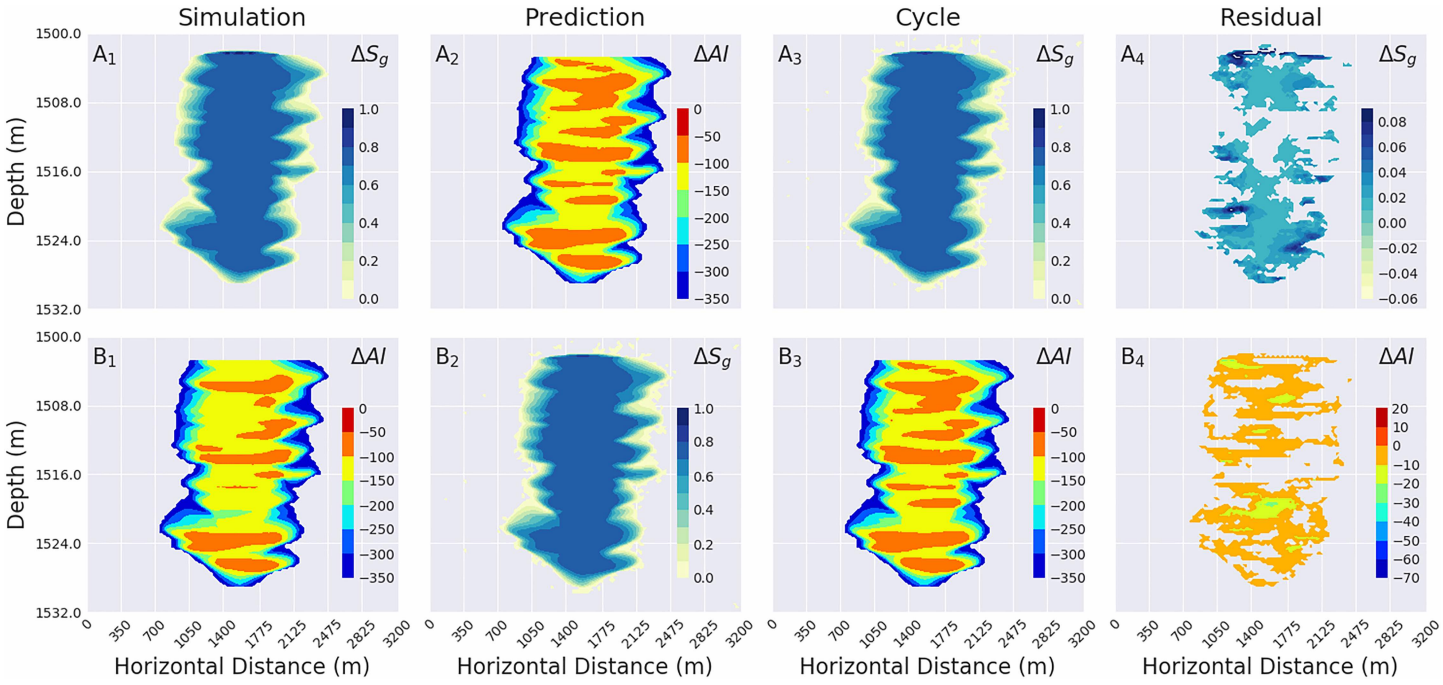

Figure 18. Illustration of the test performance for CycleGAN for one realization used in Case 2. A_1 shows the gas saturation change (ΔS_g) calculated based on the CMG simulation, A_2 shows the acoustic impedance change ($\Delta \hat{AI}$) predicted by the generative model ($G_{X\to Y}$), A_3 is the gas saturation change ($\Delta \hat{S}_g$) reconstructed by using the generative model ($G_{Y\to X}$) from predicted AI change ($\Delta \hat{AI}$), and A_4 shows the difference between A_1 and A_3. Same as Figure 5a; B_1 is the calculated AI change (ΔAI) obtained by using the rock physics models, B_2 shows the gas saturation change ($\Delta \hat{S}_g$) predicted by the generative model ($G_{Y\to X}$) from ΔAI, B_3 shows the AI change ($\Delta \hat{AI}$), which is reconstructed by the generative model ($G_{X\to Y}$) from predicted $\Delta \hat{S}_g$, and B_4 shows the difference between B_1 and B_3.

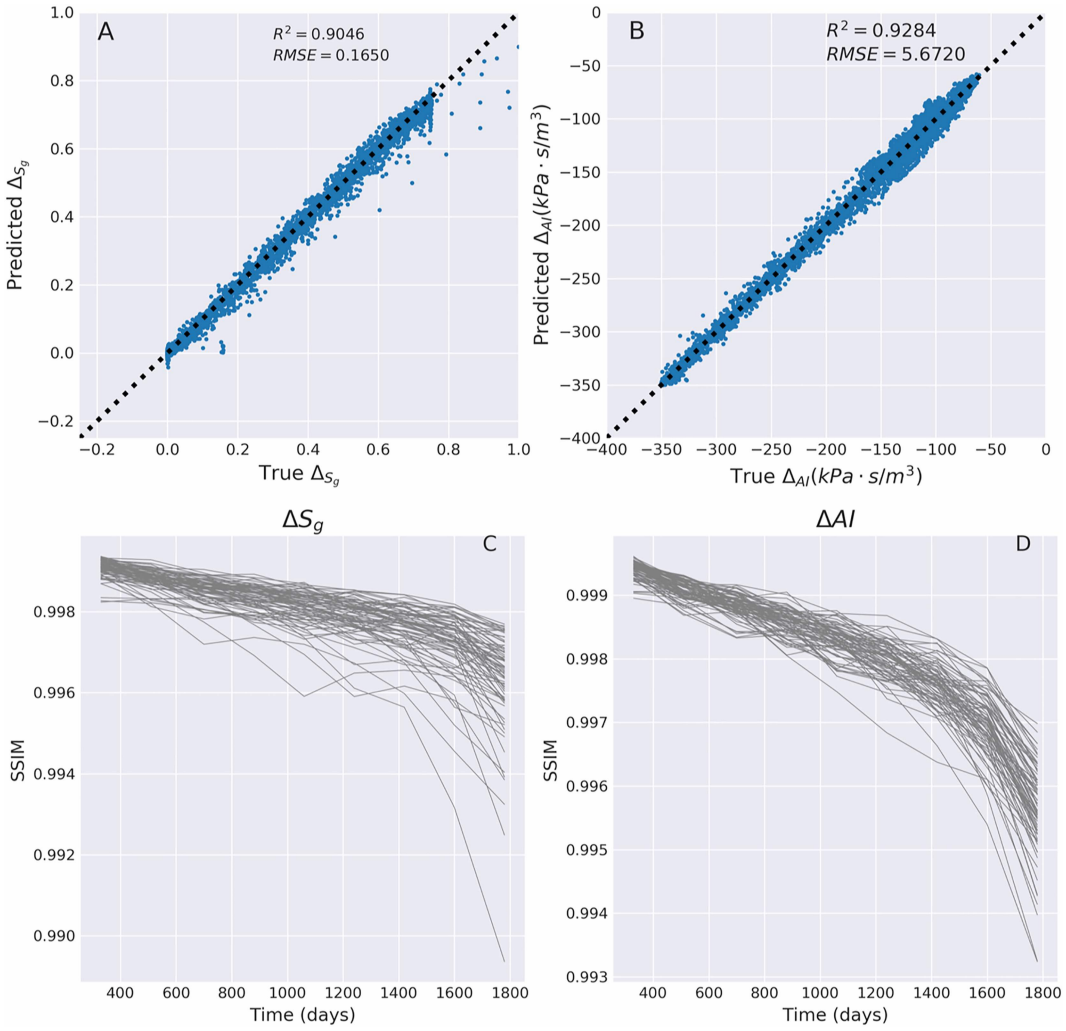

Figure 19. (a) Comparison of CMG simulation-based CO_2 saturation changes (ΔS_g) and CO_2 saturation changes ($\Delta \hat{S}_g$) reconstructed by the forward generative model ($G_{Y \to X}$) for Case 2. (b) Acoustic impedance change (ΔAI) calculated based on rock physics model and AI change ($\Delta \hat{AI}$) reconstructed by CycleGAN ($G_{X \to Y}$). (c) Plots of SSIM values obtained on the testing ensemble of 75 realizations for ΔS_g. (d) Plots of SSIM values obtained on the testing ensemble of 75 realizations for ΔAI.

can accurately predict ΔAI with a R^2 of 0.9284 and *RMSE* value of 5.6720 kPa·s/m^3. Meanwhile, the inverse generative model ($G_{Y \to X}$) can reconstruct the fluid saturation change (ΔS_g) with a R^2 of 0.9046 and *RMSE* value of 0.1650. Figure 19c shows the SSIM value between ΔS_g and $\Delta \hat{S}_g$, and Figure 19c shows the SSIM value between ΔAI and $\Delta \hat{AI}$. As Table 3 suggests, when the standard deviation value increases from the base case to Case 2, the performance (R^2 and *RMSE*) of CycleGAN is little changed for the ΔS_g prediction, but the *RMSE* between RPM calculated ΔAI and CycleGAN predicted $\Delta \hat{AI}$ increases by about 2.0 kPa·s/m^3. As Figures 18 and 19 show, the larger permeability variability has limited impact on the accuracy of Cycle-GAN prediction in this case. Again, the robust CycleGAN performance seen here can be attributed to the strong ability of CycleGAN to learn the underlying functional mappings through pattern extraction and recognition.

3.5. Impact of the Noise

To test the robustness of our proposed Cycle-GAN, we add the white noise to the testing data set and then test the performance of CycleGAN in predicting the gas saturation changes and AI changes. In this research, a Gaussian random noise with variance ($\sigma^2 = 1$) and mean magnitude of 0.1 is added into the acoustic impedance. Therefore, the acoustic impedance $AI^{noise} = AI + noise$, and the AI change is defined as

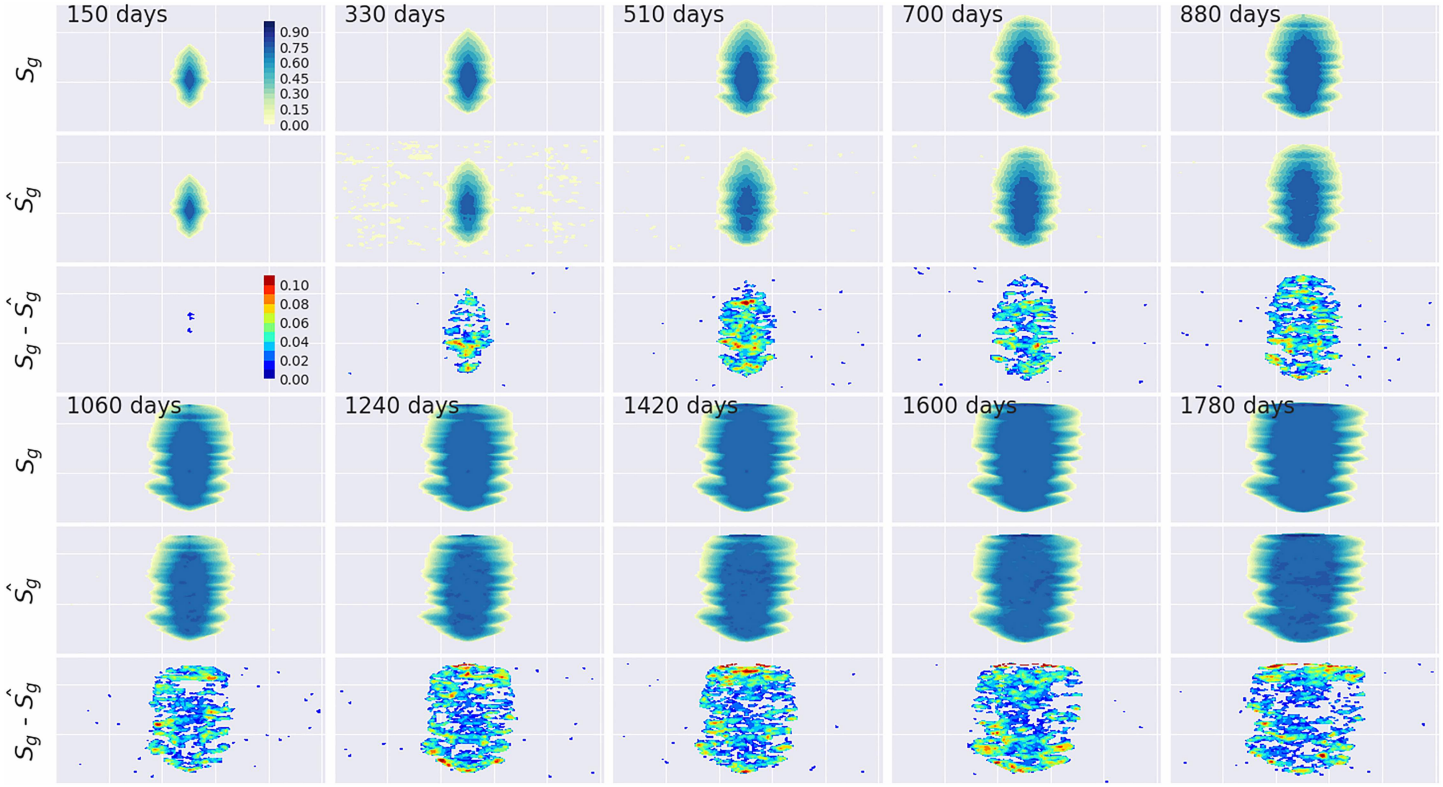

Figure 20. Snapshots of CO_2 saturation changes (ΔS_g) obtained by numerical simulation and CycleGAN model for one realization in the testing data set after adding white noise to acoustic impedance data. Top row for each panel: CO_2 saturation changes (ΔS_g) calculated based on the numerical simulation result. Middle row for each panel: CO_2 saturation changes ($\Delta \hat{S}_g$) estimated by CycleGAN model (from inverse mapping ($G_{Y\to X}$)). Bottom row of each panel: residual error maps between each pair of maps ($\Delta S_g - \Delta \hat{S}_g$).

$$\Delta AI^{\text{noise}} = (AI_2 + \text{noise}_2) - (AI_1 + \text{noise}_1),$$

$$= (AI_2 - AI_1) + (\text{noise}_2 - \text{noise}_1) \quad (33)$$

$$= \Delta AI + (\text{noise}_2 - \text{noise}_1) \quad (34)$$

$$= \Delta AI + \Delta\text{noise} \quad (35)$$

where $\text{noise}_1 \sim N(\mu, \sigma^2)$ and $\text{noise}_2 \sim N(\mu, \sigma^2)$. It can be shown that $(\text{noise}_2 - \text{noise}_1) = \Delta\text{noise} \sim N(0, 2\sigma^2)$. Therefore, a zero-mean white noise ($\Delta\text{noise} \sim N(0, 2\sigma^2)$) is actually added to the acoustic impedance changes (ΔAI).

Moreover, when AI is scaled to the range of [0,1], the magnitude of the white noise is also reduced proportionally. Figure 20 shows the CycleGAN predicted gas saturation changes using ΔAI after adding white noise to it. The top row shows the original gas saturation changes obtained by CMG simulation; middle row shows the gas saturation changes predicted using CycleGAN based on the perturbed ΔAI. The bottom row shows the difference between the true and predicted gas saturation changes. Comparing the results shown in Figures 9 and 20, it can be seen that the white noise has limited impact on the inversion. It also proves that our proposed CycleGAN is relatively robust to random (measurement) errors.

3.6. Comparison Between Traditional and Machine Learning Methods

To compare the performance of our proposed CycleGAN, we estimate the gas saturation using a traditional numerical method, and then we calculate the gas saturation changes based on equation (30) and finally we compare the inversion results obtained by the two different methods. In the current context, gas saturation inversion refers to the determination of gas saturation through the indirectly measured AI by using an iterative solver. The general workflow for this inversion process is summarized in the following four steps: (1) assigning a reasonable initial guess of the reservoir parameters, (2) calculating the variable of interest (i.e.,

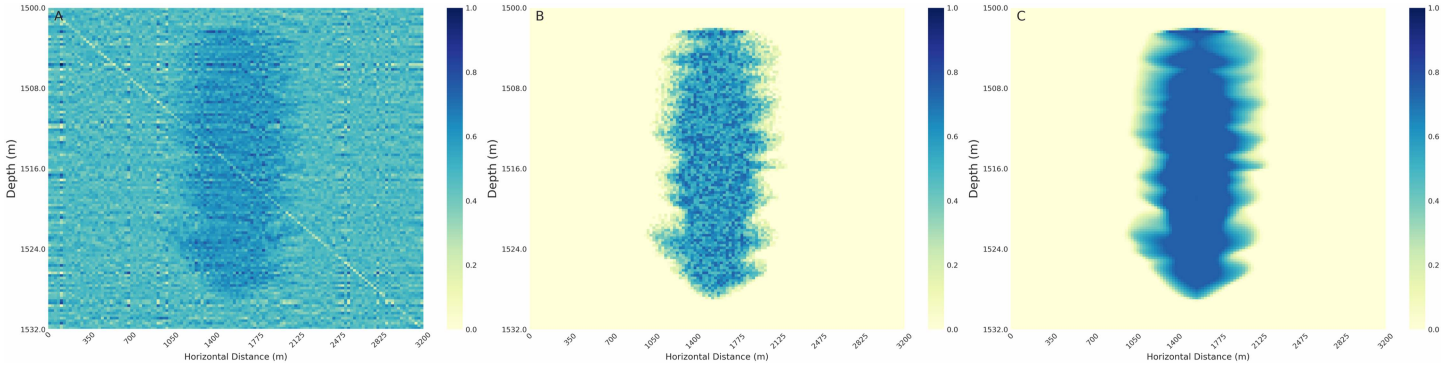

Figure 21. Gas saturation inversion using the traditional method for time 300 days for the permeability realization shown in Figure 1: (a) initial guess of gas saturation. (b) Solution obtained using Gauss-Newton iterative solver. (c) The original saturation map obtained using CMG-GEM.

AI) via the forward modeling process, (3) calculating the objective or loss function, (4) updating the reservoir parameters by minimizing the objective function defined in terms of the observed data. The process is continued until the best fit is achieved between the calculated and observed data or when the maximum number of iterations is exceeded (Dadashpour et al., 2007). In this comparison example, we apply the Gauss-Newton algorithm to minimize this objective function, and a detailed process is summarized in the supporting information (Movie S3).

Figure 21 shows the results of gas saturation based on the AI at 300 days for the permeability realization shown in Figure 1. Figure 1a shows the initial guess of gas saturation, which is a corrupted version of the "true" gas saturation given in Figure 1c. Figure 21b shows the inverted gas saturation based on the AI using the Gauss-Newton iterative solver. Here the "true" gas saturation is obtained from CMG-GEM. Because of the local nature of the gradient-based solver used here, a good initial guess of gas saturation is critically important for obtaining meaningful final solution. We tried to use a random Gaussian distribution to initialize the initial guess, but the inverted result did not converge in most situations. Thus, we simply perturbed the true gas saturation with random noise to make the iteration process converge. Although a simplistic traditional approach is applied here, we believe that the example highlights the difficulty in seismic inversion using the traditional approaches without significant constraints. As mentioned in section 1, traditional RPMs do not resolve CO_2 saturation well above a certain threshold (Zhu et al., 2019), making CO_2 mass accounting uncertain. Our CycleGAN workflow provides a potential way for refining the saturation resolution of 4-D seismic inversion through forward modeling, which is also a key contribution.

4. Discussion

This study investigates the problem of estimating bidirectional mappings between reservoir elastic property changes (AI) and fluid saturation changes using CycleGAN. We assumed that the permeability filed distribution is lognormal and then used the sequential Gaussian simulator to generate the permeability field. In practical CCS applications, significant site characterization is typically conducted before a site can be approved for carbon storage to mitigate potential risks (Sun et al., 2013, 2018). Thus, well logs, seismic data, and other survey information are available to constrain the initial geological model. In other exploratory subsurface applications, however, the distribution of permeability field may be less constrained, and the actual distribution may not be the same as the distribution of samples used in training CycleGAN. A potential strategy is to augment the training data set by including samples from multiple classes of permeability distributions. Besides the permeability, other reservoir properties (e.g., porosity, relative permeability, and lithofacies) and well schedules (e.g., injection rate and well locations) are also uncertain. The reservoir elastic property (e.g., AI) is highly dependent on lithology, and care should be taken when applying the RPM (Bachrach, 2006). Thus, physical constraints and prior knowledge are necessary to reduce the actual dimension (degree of freedom) of parameters and improve training efficiency. The RPM describes the relationship between reservoir fluid properties and reservoir rock elastic property. In this work, we assumed a single lithofacies. If more than one lithofacies is involved, the values of bulk moduli will be affected and the RPM parameters need to be modified.

The main seismic elastic property used in this research is AI, instead of seismic amplitude often collected from 4-D seismic surveys. The seismic wave attenuation caused by seismic wave energy attenuation and/or by wavefront diffusion increases the uncertainty of AI, which is inverted from seismic signal based on wave equation. This additional layer of uncertainty may limit the accuracy of our CycleGAN. Therefore, our model is only suited when the wavelet and seismic amplitude are available. On the other hand, this also provides us a tool for analyzing the uncertainty of the wavelet. To make this proposed CycleGAN applicable in more realistic settings, either AI or other elastic property should be available. Also, the training data set should be representative of the data distribution (p_Y^{data}) of domain Y, which is the main problem in the future research if more advanced machine learning algorithms are applied to solve those 2-D or 3-D time-lapse seismic inversion problems.

5. Summary and Conclusions

Recently, the CycleGAN, a type of deep learning models, has demonstrated exceptional performance for cross-domain learning. In this research, we adopt CycleGAN to build a deep learning based time-lapse seismic inversion workflow, which can be used to quickly determine reservoir fluid property changes based on time-lapse seismic data. Seismic inversion, an ill-posed and highly nonlinear problem, is traditionally solved via statistical or gradient based method, which is computationally expensive and is subject to high uncertainty. The CycleGAN-based workflow helps to solve the forward and inverse problems in seismic inversion while honoring physical constraints.

Our CycleGAN workflow is demonstrated for CO_2 plume tracking in a synthetic saline storage aquifer based on the time-lapse seismic data. In particular, forward numerical reservoir simulations are conducted by using the commercial reservoir simulator (CMG-GEM) to generate the fluid saturation properties, and rock-physical models are applied to generate seismic elastic properties based on simulated fluid saturation properties. The CycleGAN is trained to learn the bidirectional functional mappings between two domains including seismic elastic property changes (ΔAI) and reservoir fluid properties changes (ΔS_g). In the training process, ΔS_g is the input and ΔAI is the desired output in the forward training process; meanwhile, ΔAI is the input and ΔS_g is the desired output in the inversion training process.

Results show that CycleGAN achieves satisfactory performance on both the training and testing data sets, indicating that CycleGAN has a strong ability to learn the cross-domain mappings between reservoir fluid properties and seismic elastic properties. The performance of CycleGAN stays stable when the heterogeneity structure changes (e.g., smaller *logk* correlation ranges or larger *logk* standard deviation). This suggests the strong capacity of CycleGAN to adjust to the change in model hyperparameters. It should be noted that unlike many statistical or gradient-based inversion methods that require a large number of iterations, CycleGAN can conduct forward and inversion processes simultaneously and efficiently. In summary, we show that the CycleGAN workflow provides a new way for time-lapse seismic data inversion and is especially suitable for monitoring CO_2 plume migration in commercial-scale CCS projects.

Acknowledgments
We are grateful to the constructive comments by the A. E. and two anonymous reviewers, which help to improve the original manuscript significantly. A. Sun and Z. Zhong were supported by the U.S. Department of Energy, National Energy Technology Laboratory (NETL) under Grant DE-FE0026515.

References

Amini, H., & MacBeth, C. (2018). A Bayesian approach for resolving OWC and GOC from 4-D seismic data. In *80th EAGE Conference and Exhibition*.

Arts, R., Eiken, O., Chadwick, A., Zweigel, P., Van der Meer, L., & Zinszner, B. (2004). Monitoring of CO_2 injected at Sleipner using time-lapse seismic data. *Energy*, *29*(9-10), 1383–1392.

Assunção, G. S., Davolio, A., Schiozer, D. J., et al. (2016). A methodology to integrate multiple simulation models and 4-D seismic data considering their uncertainties. In *SPE Annual Technical Conference and Exhibition. Society of Petroleum Engineers*.

Bachrach, R. (2006). Joint estimation of porosity and saturation using stochastic rock-physics modeling. *Geophysics*, *71*(5), O53–O63.

Batzle, M., & Wang, Z. (1992). Seismic properties of pore fluids. *Geophysics*, *57*(11), 1396–1408.

Behzadi, H., Alvarado, V., & Mallick, S. (2011). CO_2 saturation, distribution and seismic response in two-dimensional permeability model. *Environmental Science & Technology*, *45*(21), 9435–9441.

Brie, A., Pampuri, F., Marsala, A., & Meazza, O. (1995). Shear sonic interpretation in gas-bearing sands. In *SPE Annual Technical Conference and Exhibition*, Society of Petroleum Engineers.

Cao, J., & Roy, B. (2017). Time-lapse reservoir property change estimation from seismic using machine learning. *The Leading Edge*, *36*(3), 234–238.

Castagna, J. P., & Backus, M. M. (1993). *Offset-dependent reflectivity—Theory and practice of AVO analysis*. Tulsa, OK: Society of Exploration Geophysicists.

Castagna, J. P., Batzle, M. L., & Eastwood, R. L. (1985). Relationships between compressional-wave and shear-wave velocities in clastic silicate rocks. *Geophysics*, *50*(4), 571–581.

Castelletto, N., Gambolati, G., & Teatini, P. (2013). Geological CO_2 sequestration in multi-compartment reservoirs: Geomechanical challenges. *Journal of Geophysical Research: Solid Earth*, *118*, 2417–2428. https://doi.org/10.1002/jgrb.50180

Chadwick, R., Noy, D., Arts, R., & Eiken, O. (2009). Latest time-lapse seismic data from Sleipner yield new insights into CO_2 plume development. *Energy Procedia*, *1*(1), 2103–2110.
Chan, S., & Elsheikh, A. H. (2018). Parametric generation of conditional geological realizations using generative neural networks. arXiv preprint arXiv:1807.05207.
Dadashpour, M., Landrø, M., & Kleppe, J. (2007). Nonlinear inversion for estimating reservoir parameters from time-lapse seismic data. *Journal of Geophysics and Engineering*, *5*(1), 54–66.
Dramsch, J. S., Corte, G., Amini, H., Lüthje, M., & MacBeth, C. (2019). Deep learning application for 4-D pressure saturation inversion compared to Bayesian inversion on north sea data. In *Second EAGE Workshop Practical Reservoir Monitoring* (pp. 2019).
Fu, P., Settgast, R. R., Hao, Y., Morris, J. P., & Ryerson, F. J. (2017). The influence of hydraulic fracturing on carbon storage performance. *Journal of Geophysical Research: Solid Earth*, *122*, 9931–9949. https://doi.org/10.1002/2017JB014942
Ganin, Y., Ustinova, E., Ajakan, H., Germain, P., Larochelle, H., Laviolette, F., et al. (2016). Domain-adversarial training of neural networks. *The Journal of Machine Learning Research*, *17*(1), 2096–2030.
Gassmann, F. (1951). Elastic waves through a packing of spheres. *Geophysics*, *16*(4), 673–685.
Goodfellow, I., Bengio, Y., & Courville, A. (2016). *Deep learning*. London, England: MIT Press.
Goodfellow, I., Pouget-Abadie, J., Mirza, M., Xu, B., Warde-Farley, D., Ozair, S., et al. (2014). Generative adversarial nets. In *Advances in neural information processing systems* (pp. 2672–2680).
Grana, D., & Mukerji, T. (2015). Bayesian inversion of time-lapse seismic data for the estimation of static reservoir properties and dynamic property changes. *Geophysical Prospecting*, *63*(3), 637–655.
Haszeldine, R. S. (2009). Carbon capture and storage: How green can black be? *Science*, *325*(5948), 1647–1652.
Hill, R. (1952). The elastic behaviour of a crystalline aggregate. *Proceedings of the Physical Society. Section A*, *65*(5), 349.
Hinton, G. E., Srivastava, N., Krizhevsky, A., Sutskever, I., & Salakhutdinov, R. R. (2012). Improving neural networks by preventing co-adaptation of feature detectors. arXiv preprint arXiv:1207.0580.
Isola, P., Zhu, J.-Y., Zhou, T., & Efros, A. A. (2017). Image-to-image translation with conditional adversarial networks. In *Proceedings of the IEEE conference on computer vision and pattern recognition* (pp. 1125–1134).
Jiang, X. (2011). A review of physical modelling and numerical simulation of long-term geological storage of CO_2. *Applied Energy*, *88*(11), 3557–3566.
Johansen, T. A., Jensen, E. H., Mavko, G., & Dvorkin, J. (2013). Inverse rock physics modeling for reservoir quality prediction. *Geophysics*, *78*(2), M1–M18.
Johansen, T. A., Spikes, K., & Dvorkin, J. (2004). Strategy for estimation of lithology and reservoir properties from seismic velocities and density. In *SEG Technical Program Expanded Abstracts 2004. Society of Exploration Geophysicists* (pp. 1726–1729).
Johnston, D. H. (2010). *Methods and applications in reservoir geophysics*. Tulsa, OK.
Laloy, E., Hérault, R., Jacques, D., & Linde, N. (2018). Training-image based geostatistical inversion using a spatial generative adversarial neural network. *Water Resources Research*, *54*, 381–406. https://doi.org/10.1002/2017WR022148
Ledig, C., Theis, L., Huszár, F., Caballero, J., Cunningham, A., Acosta, A., et al. (2017). Photo-realistic single image super-resolution using a generative adversarial network. In *Proceedings of the IEEE conference on computer vision and pattern recognition* (pp. 4681–4690).
Liu, M.-Y., & Tuzel, O. (2016). Coupled generative adversarial networks. In *Advances in neural information processing systems* (pp. 469–477).
Lumley, D. (2010). 4-D seismic monitoring of CO_2 sequestration. *The Leading Edge*, *29*(2), 150–155.
Maleki, M., Davolio, A., & Schiozer, D. J. (2018). Using simulation and production data to resolve ambiguity in interpreting 4-D seismic inverted impedance in the Norne Field. *Petroleum Geoscience*, *24*(3), 335–347.
Mariethoz, G., & Caers, J. (2014). *Multiple-point geostatistics: Stochastic modeling with training images*. New Jersey: John Wiley & Sons.
Mavko, G., Mukerji, T., & Dvorkin, J. (2009). *The rock physics handbook: Tools for seismic analysis of porous media*. Cambridge: Cambridge University Press.
Mosser, L., Kimman, W., Dramsch, J., Purves, S., De la Fuente Briceño, A., & Ganssle, G. (2018). Rapid seismic domain transfer: Seismic velocity inversion and modeling using deep generative neural networks. In *80th EAGE Conference and Exhibition 2018*.
Peng, D.-Y., & Robinson, D. B. (1976). A new two-constant equation of state. *Industrial & Engineering Chemistry Fundamentals*, *15*(1), 59–64.
Radford, A., Metz, L., & Chintala, S. (2015). Unsupervised representation learning with deep convolutional generative adversarial networks. arXiv preprint arXiv:1511.06434.
Remy, N., Boucher, A., & Wu, J. (2009). *Applied geostatistics with SGeMS: A user's guide*. Cambridge: Cambridge University Press.
Reuss, A. (1929). Calculation of the flow limits of mixed crystals on the basis of the plasticity of monocrystals. *Zeitschrift für angewandte Mathematik und Physik*, *9*, 49–58.
Samangouei, P., Kabkab, M., & Chellappa, R. (2018). Defense-GAN: Protecting classifiers against adversarial attacks using generative models. arXiv preprint arXiv:1805.06605.
Simm, R. (2007). Practical Gassmann fluid substitution in sand/shale sequences. *First Break*, *25*(12), 61–68.
Sun, A. Y. (2018). Discovering state-parameter mappings in subsurface models using generative adversarial networks. *Geophysical Research Letters*, *45*, 11,137–11,146. https://doi.org/10.1029/2018GL080404
Sun, A. Y., Jeong, H., González-Nicolás, A., & Templeton, T. C. (2018). Metamodeling-based approach for risk assessment and cost estimation: Application to geological carbon sequestration planning. *Computers & Geosciences*, *113*, 70–80.
Sun, N.-Z., & Sun, A. (2015). *Model calibration and parameter estimation: For environmental and water resource systems*. New York: Springer.
Sun, A. Y., Zeidouni, M., Nicot, J.-P., Lu, Z., & Zhang, D. (2013). Assessing leakage detectability at geologic CO_2 sequestration sites using the probabilistic collocation method. *Advances in Water Resources*, *56*, 49–60.
Szegedy, C., Zaremba, W., Sutskever, I., Bruna, J., Erhan, D., Goodfellow, I., & Fergus, R. (2013). Intriguing properties of neural networks. arXiv preprint arXiv:1312.6199.
Tarantola, A. (2005). *Inverse problem theory and methods for model parameter estimation* (Vol. 89). Philadelphia, PA: siam.
Tian, S., & MacBeth, C. (2015). An engineering-consistent Bayesian scheme for 4-D seismic to simulator inversion. In *77th EAGE Conference and Exhibition*.
Voigt, W. (1928). Textbook of crystal physics. BB Teubner, Leipzig 2.
Wang, Z. (1997). Feasibility of time-lapse seismic reservoir monitoring: The physical basis. *The Leading Edge*, *16*(9), 1327–1330.
Wang, Z., Bovik, A. C., Sheikh, H. R., & Simoncelli, E. P. (2004). Image quality assessment: From error visibility to structural similarity. *IEEE Transactions on Image Processing*, *13*(4), 600–612.
Yi, Z., Zhang, H., Tan, P., & Gong, M. (2017). DualGAN: Unsupervised dual learning for image-to-image translation. In *Proceedings of the IEEE International Conference on Computer Vision* (pp. 2849–2857).

Zhong, Z., & Carr, T. R. (2016). Application of mixed kernels function (MKF) based support vector regression model (SVR) for CO_2—Reservoir oil minimum miscibility pressure prediction. *Fuel*, *184*, 590–603.

Zhong, Z., & Carr, T. R. (2019). Geostatistical 3-D geological model construction to estimate the capacity of commercial scale injection and storage of CO_2 in Jacksonburg-Stringtown oil field, West Virginia, USA. *International Journal of Greenhouse Gas Control*, *80*, 61–75.

Zhong, Z., Carr, T. R., Wu, X., & Wang, G. (2019). Application of a convolutional neural network in permeability prediction: A case study in the Jacksonburg-Stringtown oil field, West Virginia, USA. *Geophysics*, *84*(6), B363–B373.

Zhong, Z., Liu, S., Kazemi, M., & Carr, T. R. (2018). Dew point pressure prediction based on mixed-kernels-function support vector machine in gas-condensate reservoir. *Fuel*, *232*, 600–609.

Zhong, Z., Sun, A. Y., & Jeong, H. (2019). Predicting CO_2 plume migration in heterogeneous formations using conditional deep convolutional generative adversarial network. *Water Resources Research*, *55*, 5830–5851. https://doi.org/10.1029/2018WR024592

Zhong, Z., Sun, A. Y., Yang, Q., & Ouyang, Q. (2019). A deep learning approach to anomaly detection in geological carbon sequestration sites using pressure measurements. *Journal of Hydrology*, *573*, 885–894.

Zhu, T., Ajo-Franklin, J., Daley, T. M., & Marone, C. (2019). Dynamics of geologic CO_2 storage and plume motion revealed by seismic coda waves. *Proceedings of the National Academy of Sciences*, *116*(7), 2464–2469.

Zhu, J.-Y., Park, T., Isola, P., & Efros, A. A. (2017). Unpaired image-to-image translation using cycle-consistent adversarial networks. In *Proceedings of the IEEE International Conference on Computer Vision* (pp. 2223–2232).